

Flux-driven algebraic damping of $m = 2$ diocotron mode

Abstract

Experiments with pure electron plasmas in a Malmberg-Penning trap have observed linear in time, algebraic damping of $m = 2$ diocotron modes. Transport due to small field asymmetries produces a low density halo of electrons moving radially outward from the plasma core, and the mode damping begins when the halo reaches the resonant radius of the mode. The damping rate is proportional to the flux of halo particles through the resonant layer. The damping is related to, but distinct from spatial Landau damping, in which a linear wave-particle resonance produces exponential damping. This paper reports an analytic theory that captures the main signatures reported for this novel damping: namely, that the damping begins when the halo particles reach the resonant radius and that the damping is algebraic in time with nearly constant damping rate. The model also predicts a nonlinear frequency shift. The model provides two ways to think about the damping. It results from a transfer of canonical angular momentum from the mode to halo particles being swept by the mode field through the nonlinear cat's-eye orbits of the resonant region. More mechanistically, the electric field produced by the perturbed charge density of the resonant particles acts back on the plasma core causing $\mathbf{E} \times \mathbf{B}$ -drift that give rise to the damping and nonlinear frequency shift.

1 Introduction

Diocotron modes are dominant features in the low frequency dynamics of nonneutral plasmas confined in Malmberg-Penning traps.^{1–4} In an ideal limit, these modes involve only cross magnetic field $\mathbf{E} \times \mathbf{B}$ drift motion and are described by the drift-Poisson equations.¹ These equations are isomorphic to the Euler equations for the ideal, that is, incompressible and inviscid) flow of a neutral fluid, and the diocotron modes are analogues of Kelvin modes on a fluid vortex.^{5,6}

There has been much previous work on diocotron mode instabilities^{2,7–9} and on diocotron mode damping.^{5,6,10–13} This paper focuses on damping.

Previously identified damping mechanisms include a spatial version of the Landau resonance,^{5,10} the rotational pumping of bulk viscosity,^{11,12} axial velocity dissipation on a separatrix for plasma columns with trapped and passing particles,¹⁴ and a strong damping mechanism when the radial magnetron

field from end cylinders dominates over the radial space charge field.¹³ The Landau mechanism fits into the ideal 2D $\mathbf{E} \times \mathbf{B}$ drift framework, but others, such as rotational pumping, involve physics beyond the ideal model.

This paper discusses a damping mechanism that is a close cousin of Landau damping, so we begin with a review of the spatial Landau resonance.

In accord with the experiments, we consider a nonneutral plasma column that is confined in the uniform axial magnetic field $B\hat{z}$ of a Malmberg-Penning trap. Let (r, θ, z) be a cylindrical coordinate system with the z-axis coincident with the axis of the trap. Because the plasma is unneutralized, there is a radial space charge electric field $E(r)\hat{r}$. The cross magnetic field motion is well described in the drift approximation, and the plasma undergoes azimuthal $\mathbf{E} \times \mathbf{B}$ drift rotation. A diocotron mode of azimuthal mode number m can experience a resonant interaction with the rotating plasma flow at the critical plasma radius R_m , where $\omega_m = m\omega_E(R_m)$. Here, ω_m is the mode frequency, and $\omega_E(r) = -cE(r)/Br$ is the local rotation frequency of the plasma.

Linear mode theory^{5,10} predicts that this spatial Landau resonance produces exponential mode damping when the slope of the radial density distribution is negative at the critical radius, and this damping has been observed experimentally.¹⁰

Recent experiments¹⁵ have observed a novel algebraic damping of the $m = 1$ and $m = 2$ diocotron mode, which we believe is a close cousin of spatial Landau damping. In these experiments, transport produces a low density halo of particles that gradually extends out from the plasma core. The damping is reported¹⁵ to begin when the halo reaches the resonant radius and to be algebraic in time dependence with a nearly constant damping rate. The time dependence for the mode amplitudes is well fit by the expressions

$$D_1(t) = D_1(t_1) - \gamma_1(t - t_1), \quad (1)$$

$$D_2(t) = D_2(t_2) - \gamma_2(t - t_2), \quad (2)$$

where $D_1(t)$ and $D_2(t)$ are the amplitudes of modes $m = 1$ and $m = 2$, t_1

and t_2 are the times when the expanding halo reaches the resonant radius for modes 1 and 2, and the secular damping rates γ_1 and γ_2 are nearly constant damping rates.

The theoretical picture that we envision for this flux driven algebraic damping is similar to, but distinct from, spatial Landau damping. In both cases, the damping results from an interaction of the mode field with resonant particles, but the particulars of the interactions are very different in the two cases. In spatial Landau damping, the resonant particles are present before the mode is excited, and the damping results from a mode-driven rearrangement of particles near the resonant radius. The analysis is linear and leads to exponential damping.

In contrast, for the new flux-driven algebraic damping, there are no particles initially at the resonant radius. The transport gradually brings particles to the resonant radius, the mode field then sweeps these particles across the nonlinear cat's eye region, transferring canonical angular momentum to the

particles and the mode damps in response.

Before proceeding to a discussion of the damping mechanism, we note that the transport mechanism which creates the halo is not well understood. The halo transport is thought to be due to the transfer of angular momentum to the plasma from static field errors; the halo flux can be increased by imposing additional field asymmetries. In the experiments, an electron halo is observed by dumping the plasma out along the field lines to a phosphorus screen.¹⁵ Good shot-to-shot reproducibility is used to construct a time evolution, by dumping at a sequence of times after plasma injection.

At the time of the original experiments,¹⁵ the nonneutral plasma was thought to consist exclusively of electrons, but it was difficult to understand how field error transport would pull out a low density halo of electrons, rather than expand the plasma column as a whole. More recent experiment suggest that the plasma consists of electrons plus a few percent admixture of negative hydrogen ions.¹⁶ Thus, the halo may consist of negative ions, which have a

much lower axial bounce frequency than the electrons and can experience enhanced field error transport due to resonance between the axial bounce motion and the $\mathbf{E} \times \mathbf{B}$ drift rotational motion.¹⁷ An experimental complication is that the phosphorous screen registers only the electrons, not ions, so one must envision a process that involves transport of negative ions followed by photo-dissociation of negative ions to produce the electron halo seen by the screen.

For the theoretical model of the damping and nonlinear frequency shift considered here, the halo can consist of either electrons or of negative ions, since both species undergo the same $\mathbf{E} \times \mathbf{B}$ drifts. However, in comparing the predicted damping rate to the measured damping rate, there may be a small uncertainty concerning the halo density and flux inferred from the phosphorous screen images of the electrons.

Ref. 21 provides a theoretical treatment of the flux-driven damping and an associated nonlinear frequency shift for the $m = 1$ mode, and this paper

provides such a treatment for the $m = 2$ mode. Because both modes undergo linear in time, algebraic damping and because the damping mechanism for both modes involves a transfer of canonical angular momentum to resonant particles, one might expect the theory for the $m = 2$ mode to be a trivial extension of that for the $m = 1$ mode. However, that is not the case. As we will see, an effect that provides only a small correction to the damping for the $m = 1$ mode plays a crucial role in establishing the linear in time nature of algebraic damping for the $m = 2$ mode.

To understand the damping mechanism in more detail and to understand the difference between the damping for the $m = 1$ and $m = 2$ modes, we review a simple heuristic treatment of the damping given in the publication that reported the experimental results.¹⁵ Fig. (1a) shows the cross-section of a pure electron plasma when an $m = 1$ diocotron mode has been excited, and Fig. (1b) shows the cross-section when an $m = 2$ diocotron mode has been excited. The plasma consists of a high density core, shown as the orange

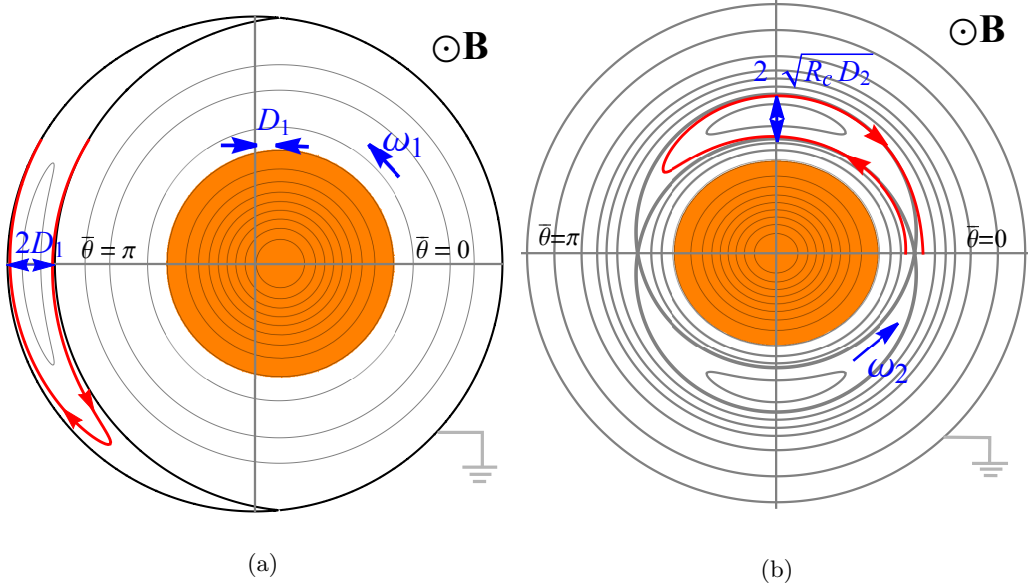


Figure 1: Cross sections of the electron plasma column when (a) $m = 1$ and (b) $m = 2$ modes have been excited. The orange shaded region is the plasma core. The gray lines are equipotential contours. The red line is a resonant particle trajectory.

regions in the figures, and a much lower density halo extending out from the core.

For simplicity, the unperturbed density profile, $n^{(0)}(r)$, is taken here to be the top-hat form. The unperturbed density in the core is uniform out to some radius R_c and then drops abruptly to the much lower value of the halo density. Because the $\mathbf{E} \times \mathbf{B}$ -drift flow is incompressible, the core density remains uniform even when the mode is excited. The core surface simply

distorts.

The grey curves are equipotential contours, as seen in the rotating frames of the modes. For sufficiently weak transport and damping, the $\mathbf{E} \times \mathbf{B}$ -drift flow is nearly along these contours. Near the core, the contours are well described by linear mode theory. In Fig. (1a), these contours are circles displaced off the trap axis. The contour that describes the surface of the core is

$$r_s(\bar{\theta}_1) = R_c + D_1 \cos \bar{\theta}_1, \quad (3)$$

where $\bar{\theta}_1 = \theta - \omega_1 t - \alpha_1$ is the angle measured in the rotating frame of the mode. Likewise, in Fig. (1b) the linear contours are elliptically distorted circles, and the surface of the core is given by

$$r_s(\bar{\theta}_2) = R_c + D_2 \cos 2\bar{\theta}_2, \quad (4)$$

where $\bar{\theta}_2 = \theta - \omega_2 t/2 - \alpha_2/2$ is the angle in the rotating frame of the mode. The outermost equipotential, which is a circle of radius $r = R_w$, is coincident

with the conducting wall bounding the confinement region of the trap. Of course, the conducting wall is an equipotential.

The resonant layer for the $m = 1$ mode is at the wall radius, $R_1 = R_w$, and in this region of Fig. (1a) nonlinearity distorts the equipotential contours. One can see the cat's eye orbits adjacent to the wall on the Left Hand Side of Fig. (1a). In general cat's eye orbits are closed and describe the motion of particles that are trapped in the troughs of the wave.

For the top-hat density profile, the resonant layer for the $m = 2$ mode is at the radius $R_2 \simeq \sqrt{2}R_c$, and one can see two sets of cat's eye orbits at this radius in Fig. (1b).

In addition to the $\mathbf{E} \times \mathbf{B}$ -drift flow there is a slow radial transport flow. The transport flow produces the low density halo that extends out from the plasma core to the wall, where particles (electrons) are absorbed. Over most of the halo, the transport flow is dominated by mobility. In the region of linear equipotential contours, a given particle spirals radially outward, under

the combined action of the $\mathbf{E} \times \mathbf{B}$ -drift and mobility flow, moving successively from one equipotential contour to another of larger circumference.

The solid red curve in Fig. (1a) shows the trajectory of a particle that is being swept around the edge of the cat's eye region to the wall, where the particle is absorbed. Likewise, the solid red curve in Fig. (1b) shows a particle that is being swept around the edge of the cat's eye region.

In Fig. (1a), the passage around the edge of the cat's eye region is one-way, since the trajectory is truncated by the wall. In Fig. (1b), the passage also is one way, since the outward transport flow prevents the particle from re-entering the cat's eye region.

As mentioned earlier, the damping results from a transfer of canonical angular momentum from the mode to the particles being swept around the cat's eye orbits. In the guiding center drift approximation, the canonical angular momentum for an electron in the uniform magnetic field of the trap is simply $P_\theta = eBr^2/2c$, where the radial position r is measured from the

center of the trap, B is the magnetic field strength, and $e = -|e|$ is the electron charge.^{18,19} When an $m = 1$ diocotron mode is excited, the plasma core is displaced off the axis by the small distance D_1 , and the core angular momentum per unit length is changed by the amount $N e B D_1^2 / (2c)$, where N is the number of core particles per unit length. This change is called the canonical angular momentum per unit length of the $m = 1$ mode. For the simple case of the top-hat core, the canonical angular momentum per unit length for the $m = 2$ mode is $N e B D_2^2 / (2c)$.¹⁰

First let us consider angular momentum transfer for the case of $m = 1$ mode. When a halo particle $\mathbf{E} \times \mathbf{B}$ -drifts in a nearly circular orbit around the displaced center of the plasma core, the radial position of the particle measured from the center of the trap oscillates by $\Delta r(t) \simeq D_1 \cos \theta(t)$. Thus, the particle continually trades angular momentum back and forth with the mode. However, when the particle makes a one way passage around the cat's eye orbits to the wall, there is a net transfer of canonical angular momentum

to the particle. Since the thickness of the cat's eye region is of order D_1 , the

change in electron canonical angular momentum is of order

$$\Delta P'_\theta = (eB/2c)[R_w^2 - (R_w - D_1)^2] \simeq (eB/c)R_wD_1. \quad (5)$$

The precise radial displacement of the particle as it is swept through the cat's

eye orbit depends on the angle $\bar{\theta}_1$ at which the particle passes through the

separatrix for the cat's eye region, and the heuristic treatment in previous

publications^{15,20} obtained the average change in canonical angular momentum

$$\langle \Delta P_\theta \rangle_1 = (2/\pi)(eB/c)R_wD_1. \quad (6)$$

Balancing the rate of change of mode angular momentum against the rate

of change of halo particle angular momentum yields the equation

$$\frac{d}{dt}N\frac{eB}{2c}D_1^2 + \left| \frac{dN}{dt} \right| \langle \Delta P_\theta \rangle_1 = 0, \quad (7)$$

where $|dN/dt|$ is the rate per unit length at which halo particles pass through

the resonance to the wall. Substituting for $\langle \Delta P_\theta \rangle_1$ and neglecting the deriva-

tive of N in the first term yields the damping rate equation

$$\frac{dD_1}{dt} = -\frac{2}{\pi} \frac{1}{N} \left| \frac{dN}{dt} \right| R_w = -\gamma_1, \quad (8)$$

with a solution of linear algebraic damping as given by Eq. (1), with

$$\gamma_1 = \frac{2}{\pi} \frac{1}{N} \left| \frac{dN}{dt} \right| R_w. \quad (9)$$

The same argument may be applied to the $m = 2$ mode, except that for this case the width of the cat's eye orbits is $\sqrt{R_c D_2}$, leading to the average change in angular momentum $\langle \Delta P_\theta \rangle_2 = (4/\pi)(eB/c)R_c\sqrt{2R_c D_2}$. Angular momentum balance then yields the damping rate

$$\frac{dD_2}{dt} = -\frac{4}{\pi} \sqrt{\frac{2R_c}{D_2}} R_c \frac{1}{N} \left| \frac{dN}{dt} \right| \quad (10)$$

and the solution

$$\frac{2}{3}[D_2(t)]^{3/2} = \frac{2}{3}[D_2(t_2)]^{3/2} - \frac{4}{\pi} R_c^{3/2} \frac{1}{N} \left| \frac{dN}{dt} \right| (t - t_2), \quad (11)$$

which differs in form from Eq. (2).

The difference between the solutions for the $m = 1$ and $m = 2$ modes also is apparent in damping rates (8) and (10) for the two modes. Damping rate

(8) is a constant, as is required for linear algebraic damping that is linear in time, but damping rate (10) scales as $1/\sqrt{D_2(t)}$, becoming large as $D_2(t)$ becomes small.

For simplicity, the heuristic discussion¹⁵ treated the mode amplitude as constant for the orbit calculations, which is an acceptable approximation for weak damping, but not for damping rate (10) at small values of $D_2(t)$. This is why solution (11) fails to capture the observed linear in time, algebraic damping rate.

When the mode amplitude decreases, the width of the cat's-eye region decreases. In particular, the radially inner separatrix moves radially outward. When this outward motion of the separatrix is faster than the radially outward transport flow, particles are no longer swept around the cat's-eye region and the damping is turned off. In this way, a negative feedback mechanism sets up a balance that keeps the damping rate for the $m = 2$ mode nearly constant, yielding the observed linear in time, algebraic damping.

The feedback mechanism also operates for the $m = 1$ mode, but for this mode, the zeroth order damping rate in Eq. (8) is small and constant, and the feedback yields only a small correction.

Another difference between the $m = 1$ and $m = 2$ modes is that for the $m = 2$ mode there is a halo density flow in the region beyond the cat's eye orbits, that is, in the region between the cat's eye orbits and the wall in Fig. (1b). As we well see, the flow in this region is very complicated. In a zero diffusion model, the flow is characterized by an interlaced filamentary structure. Diffusion smooths this complicated structure, but the halo density is reduced relative to that on the inner side of the cat's eye region.

As noted in the theory paper for the $m = 1$ mode,²¹ the heuristic theory description in the original publication¹⁵ is inadequate in many ways. First the description leaves questions unanswered. Given that the resonant particles cause mode damping, do they also cause a nonlinear frequency shift? We will see that the answer is yes. Also, the heuristic theory focuses on a thin ribbon

of particles being swept around the cat's eye orbits, but there are many more resonant particles. Is it really true that these other resonant particles make negligible contribution to the damping?

A conceptual issue is the use of angular momentum balance. In fact, the total angular momentum of the core and halo is not conserved. Transport continually changes the angular momentum of the halo particles as the particles move radially outward.

Also, the heuristic theory uses a zero diffusion idealization; the transport is assumed to be due exclusively to a mobility flux. However, for the experimental conditions, diffusion affects the orbits of all the particles deemed responsible for the damping. Indeed, the whole idea of well-defined orbits loses meaning when diffusion is taken into account. The orbits are diffusively broadened.

What is needed is a more rigorous theory based on a solution of the coupled Poisson and transport equations. Such a theory talks about an evolving

density distribution, rather than particle orbits, and makes no assumption concerning conservation of angular momentum. Ref. 19 developed such a theory for the $m = 1$ mode, and here we develop such a theory for the $m = 2$ mode.

2 Integral expressions for the damping rate and nonlinear frequency shift

This section obtains formal expressions for the damping rate and nonlinear frequency shift as Green's function integrals over the halo density distribution. In obtaining these expressions, the perturbed charge density of the core is assumed to evolve according to linear $\mathbf{E} \times \mathbf{B}$ -drift theory. The evolution of the halo density is more complicated, involving both transport flow and nonlinear $\mathbf{E} \times \mathbf{B}$ -drift flow, and is deferred to a later section.

The Green's function integrals represent the potential due to the perturbed charge density of the halo, and one can view the damping and frequency shift as arising from $\mathbf{E} \times \mathbf{B}$ -drifts produced by the halo potential acting back on the plasma core. A previous publication²² developed this way of viewing the damping and frequency shift and we follow that analysis here.

As mentioned in the introduction, the case of a top hat profile is particu-

larly simple because the incompressible -drift flow cannot change the value of

the density within the core; the flow simply distorts the surface of the core.

Using the linear expression for the distorted surface and allowing a slow time

dependence in the amplitude $D_2(t)$ and phase $\alpha_2(t)$ yields the expression

$$r_s(\theta, t) = R_c + D_2(t) \cos[2\theta - \omega_2 t - \alpha_2(t)], \quad (12)$$

where $r_s(\theta, t)$ is the radial location of the distorted surface. The linearized

total time derivative of $r_s(\theta, t)$ is given by the expression

$$\begin{aligned} \frac{d}{dt} r_s(\theta, t) &= \left[\frac{\partial}{\partial t} + \omega_E(R_c) \frac{\partial}{\partial \theta} \right] r_s(\theta, t) \\ &= [\omega_2 + \dot{\alpha}_2(t) - 2\omega_E(R_c)] D_2(t) \sin[2\theta - \omega_2 t - \alpha_2(t)] \\ &\quad + \dot{D}_2(t) \cos[2\theta - \omega_2 t - \alpha_2(t)]. \end{aligned} \quad (13)$$

Since the motion of the surface is due to $\mathbf{E} \times \mathbf{B}$ -drift caused by the mode

potential, we can also write the time derivative as the drift velocity

$$\frac{d}{dt} r_s(\theta, t) = -\frac{c}{BR_c} \frac{\partial}{\partial \theta} \delta\phi(R_c, \theta, t), \quad (14)$$

where $\delta\phi(r, \theta, t)$ is the mode potential.

The $m = 2$ Fourier component of the mode potential and the density perturbation are related by the Green's function integral¹⁰

$$\delta\phi_2(r, t) = -4\pi e \int_0^{R_w} 2\pi r' dr' G_2(r, r') \delta n_2(r', t), \quad (15)$$

where

$$G_2(r, r') = \frac{1}{8\pi} \begin{cases} \frac{r^2}{r'^2} \left(\frac{r'^4}{R_w^2} - 1 \right) & \text{for } r < r' \\ \frac{r'^2}{r^2} \left(\frac{r^4}{R_w^2} - 1 \right) & \text{for } r > r' \end{cases} \quad (16)$$

is the Green's function and R_w is the wall radius. Of course, the Green's function vanishes at $r = R_w$.

It is convenient to write the perturbed density as the sum of a term from the core region and a term from the halo region, $\delta n(r, \theta, t) = \delta n_c(r, \theta, t) + \delta n_h(r, \theta, t)$. Likewise we write the potential as the sum $\delta\phi(r, \theta, t) = \delta\phi_c(r, \theta, t) + \delta\phi_h(r, \theta, t)$, where $\delta\phi_c$ is produced by the charge density $e\delta n_c$, and $\delta\phi_h$ is produced by the charge density $e\delta n_h$.

By recalling that the core density takes the uniform value n_c out to $r = r_s(\theta, t)$ and then drops to the much lower density n_h , we see that the linear

perturbed core density is simply

$$\delta n_c = (n_c - n_h) D_2(t) \cos[2\theta - \omega_2 t - \alpha_2(t)] \delta(r - R_c), \quad (17)$$

where $\delta(r - R_c)$ is a delta function. The Green's function integral then yields

the core potential

$$\delta\phi_c(R_c, \theta, t) = -\pi e(n_c - n_h) R_c \left(\frac{R_c^4}{R_w^4} - 1 \right) D_2(t) \cos[2\theta - \omega_2 t - \alpha_2(t)]. \quad (18)$$

Combining Eqs. (13) and (14) and substituting for $\delta\phi_c(R_c, \theta, t)$ yields the

equation

$$\begin{aligned} & -\frac{c}{BR_c} \frac{\partial}{\partial\theta} \delta\phi(R_c, \theta, t) - \frac{2\pi ec}{B} (n_c - n_h) R_c \left(\frac{R_c^4}{R_w^4} - 1 \right) D_2(t) \sin[2\theta - \omega_2 t - \alpha_2(t)] \\ &= [\omega_2 + \dot{\alpha}_2(t) - 2\omega_E(R_c)] D_2(t) \sin[2\theta - \omega_2 t - \alpha_2(t)] \\ &+ \dot{D}_2(t) \cos[2\theta - \omega_2 t - \alpha_2(t)]. \end{aligned} \quad (19)$$

It is instructive to examine this equation first in the case where there is no resonant halo interaction and \dot{D}_2 , $\dot{\alpha}_2$ and $\delta\phi_h$ are all zero. This equation then implies the dispersion relation for an $m = 2$ diocotron mode on a top-hat

density profile

$$\omega_2 - 2\omega_E(R_c) = -\omega_E(R_c) \left(1 - \frac{n_h}{n_c}\right) \left(1 - \frac{R_c^4}{R_w^4}\right), \quad (20)$$

where use has been made of the relation $\omega_E(R_c) = -2\pi n_c ec/B$. This dispersion relation is well known in the limit $n_h/n_c \rightarrow 0$.¹ By using Eq. (20) as the definition of ω_2 , Eq. (19) yields the result

$$-\frac{c}{BR_c} \frac{\partial}{\partial \theta} \delta\phi(R_c, \theta, t) = \dot{\alpha}_2(t) D_2(t) \sin[2\theta - \omega_2 t - \alpha_2(t)] + \dot{D}_2(t) \cos[2\theta - \omega_2 t - \alpha_2(t)]. \quad (21)$$

Thus, the slow rate of change of the mode amplitude $\dot{D}_2(t)$ and the small frequency shift $\Delta\omega_2 = \dot{\alpha}_2(t)$ are produced by drifts from the halo potential acting back on the surface of the core

$$\begin{aligned} \dot{D}_2(t) &= - \int_0^{2\pi} \frac{d\bar{\theta}_2}{\pi} \frac{c}{BR_c} \frac{\partial}{\partial \bar{\theta}_2} \delta\phi_h(R_c, \bar{\theta}_2) \cos 2\bar{\theta}_2 \\ &= - \frac{2c}{BR_c} \int_0^{2\pi} \frac{d\bar{\theta}_2}{\pi} \delta\phi_h(R_c, \bar{\theta}_2) \sin 2\bar{\theta}_2, \end{aligned} \quad (22)$$

$$\begin{aligned} D_2 \dot{\alpha}_2(t) &= - \int_0^{2\pi} \frac{d\bar{\theta}_2}{\pi} \frac{c}{BR_c} \frac{\partial}{\partial \bar{\theta}_2} \delta\phi_h(R_c, \bar{\theta}_2) \sin 2\bar{\theta}_2 \\ &= \frac{2c}{BR_c} \int_0^{2\pi} \frac{d\bar{\theta}_2}{\pi} \delta\phi_h(R_c, \bar{\theta}_2) \cos 2\bar{\theta}_2, \end{aligned} \quad (23)$$

where $\bar{\theta}_2 = \theta - \omega_2 t/2 - \alpha_2(t)/2$ is the angle in the rotating frame of the mode.

Using the Green's function expression for the halo potential yields the results

$$\dot{D}_2(t) = \frac{ec}{BR_c} \int_0^{2\pi} \frac{d\bar{\theta}_2}{\pi} \int_{R_c}^{R_w} 2\pi r' dr' \frac{R_c^2}{r'^2} \left(\frac{r'^4}{R_w^4} - 1 \right) n_h(r', \bar{\theta}_2, t) \sin 2\bar{\theta}_2, \quad (24)$$

$$D_2 \dot{\alpha}_2(t) = -\frac{ec}{BR_c} \int_0^{2\pi} \frac{d\bar{\theta}_2}{\pi} \int_{R_c}^{R_w} 2\pi r' dr' \frac{R_c^2}{r'^2} \left(\frac{r'^4}{R_w^4} - 1 \right) n_h(r', \bar{\theta}_2, t) \cos 2\bar{\theta}_2. \quad (25)$$

Here, the form of the Green's function for $r' > r$ has been used, and $n_h(r', \bar{\theta}_2, t)$

is the halo density in the rotating frame of the mode. We will solve for this

density in subsequent sections.

This is a good point to return to the question of angular momentum balance. Multiplying Eq. (24) by $\pi(n_c - n_h)R_c^2 eBD_2/c$ and using Eqs. (17), (18) and (22) allows Eq. (24) to be rewritten as the statement that the torque exerted by $\delta\phi_c$ on δn_h is equal and opposite to the torque exerted by $\delta\phi_h$ on δn_c . Two opposing torques are equal and opposite, even if a third

torque acts. Here, the third torque is associated with transport, which moves particles radial outward increasing their angular momentum. The transport continually increases the total angular momentum of the core and halo, but the internal torques of the core on the halo and the halo back on the core balance. The Green's function solution correctly focuses on torque balance rather than angular momentum balance.

3 Transport equation

In the halo region, the particles move under the combined influence of an $\mathbf{E} \times \mathbf{B}$ -drift flow and a radial transport flow, so that density evolves according to the equation

$$\frac{\partial n_h}{\partial t} + \frac{c}{B} \hat{z} \times \nabla_{\perp} \phi \cdot \nabla_{\perp} n_h + \frac{1}{r} \frac{\partial}{\partial r} r \Gamma_r(r) = 0, \quad (26)$$

where $\phi(r, \theta, t)$ is the total electric potential and $\Gamma_r(r)$ is the radial transport flux.

We employ a Hamiltonian description of the drift dynamics, where $H(\theta, P_{\theta}, t) = e\phi[r(P_{\theta}), \theta, t]$ is the Hamiltonian and $(\theta, P_{\theta} = eBr^2/2c)$ are a canonically conjugate coordinate and momentum pair.^{19,23,24} Here, use has been made of the fact that the trap magnetic field is axial and uniform. One can check that Hamilton's equations of motion²⁵ yield the $\mathbf{E} \times \mathbf{B}$ -drift velocity. The first two terms on the Left Hand Side of Eq. (26) then can be written in the

form

$$\frac{\partial n_h}{\partial t} + \frac{c}{B} \hat{z} \times \nabla_{\perp} \phi \cdot \nabla_{\perp} n_h = \frac{\partial n_h}{\partial t} + [n_h, H], \quad (27)$$

where $[n_h, H]$ is a Poisson bracket.²⁶

On general grounds, the flux is expected to be of the Fick's Law form²⁷

$$\Gamma_r = -\mu \frac{\partial \phi^{(0)}}{\partial r} n - \mathcal{D} \frac{\partial n}{\partial r}, \quad (28)$$

where the coefficient of mobility μ and the diffusion coefficient \mathcal{D} satisfy the

Einstein relation, $\mu = e\mathcal{D}/T$. Here, $-\partial \phi^{(0)}/\partial r$ is the unperturbed radial

electric field and T is the temperature in the halo region. For the definitions of μ and \mathcal{D} in Eq. (28), μ is positive for positively charged species

and negative for negatively charged species (i.e., for electrons); \mathcal{D} is positive for both positive and negative species. Thus, for electrons, both sides

of the Einstein relation are negative. The Fick's Law form follows from the

requirement that the flux vanishes for the thermal equilibrium density profile, $n(r) = n^{(0)} \exp[-e\phi^{(0)}(r)/T]$. Here, we use the assumption that the field

asymmetries causing the transport are static in the laboratory frame; the thermal equilibrium state is possible only in a frame where the asymmetries are static.

By changing variables from (r, θ, t) to (θ, P_θ, t) , Eq. (27) takes the form

$$\frac{\partial n}{\partial t} + [n, H] = \frac{\partial}{\partial P_\theta} \left[-\dot{P}_\theta|_T n + \tilde{\mathcal{D}} \frac{\partial n}{\partial P_\theta} \right], \quad (29)$$

where

$$\dot{P}_\theta|_T = -\mu \frac{eB}{c} r \frac{\partial \phi^{(0)}}{\partial r}, \quad \tilde{\mathcal{D}} = -\frac{2T \dot{P}_\theta|_T P_\theta}{er \partial \phi^{(0)} / \partial r}. \quad (30)$$

Here $\dot{P}_\theta|_T$ is the rate at which mobility changes the value of P_θ for a particle.

Note that both P_θ and $\dot{P}_\theta|_T$ are negative for electrons and that $\tilde{\mathcal{D}}$ is positive independent of the sign of the charge species.

Since the number of halo particles is small compared to the number of core particles, $er \partial \phi^{(0)} / \partial r$ is approximately $-2Ne^2$, where N is the number per unit length of particles in the core. Thus, we find the ratio

$$\frac{\tilde{\mathcal{D}}}{\dot{P}_\theta|_T} = -P_\theta \frac{T}{Ne^2}, \quad (31)$$

where T/Ne^2 is small for the conditions of the experiment (i.e. 10^{-3} to 10^{-2}).

Consequently, diffusion is small compared to mobility unless the local density gradient is very large [i.e., $(\partial n/\partial P_\theta)(P_\theta/n) \sim Ne^2/T \gg 1$].

As noted in Section 2, it is convenient to work in the rotating frame of the mode. The generating function²⁶

$$F(\theta, P_\theta, t) = \bar{P}_\theta \left[\theta - \frac{\omega_2 t + \alpha_2(t)}{2} \right] \quad (32)$$

yields a canonical transformation to this rotating frame, with the new coordinate and momentum

$$\bar{\theta}_2 = \theta - \frac{\omega_2 t + \alpha_2(t)}{2}, \bar{P}_\theta = P_\theta \quad (33)$$

and the new Hamiltonian

$$\bar{H} = H + \frac{\partial F}{\partial t} = H - \frac{\omega_2 + \Delta\omega(t)}{2} P_\theta, \quad (34)$$

where $\Delta\omega(t) \equiv \dot{\alpha}_2(t)$ is the nonlinear frequency shift. Since \bar{P}_θ and P_θ are equal, we continue to use P_θ in the new Hamiltonian. To work in the rotating frame, one need to only replace H by \bar{H} in Eq. (29), the Right Hand Side of

the equation needs not be changed since the radial flux is the same in both frames.

Since the transport flow is slow compared with the $\mathbf{E} \times \mathbf{B}$ -drift flow, the halo particles very nearly follow curves of constant \bar{H} . Thus, changing independent variables from $(\bar{\theta}_2, P_\theta, t)$ to $(\bar{\theta}_2, \bar{H}, t)$ in Eq. (29) is useful. The result is the transport equation

$$\begin{aligned} \frac{\partial n}{\partial t} \Big|_{\bar{\theta}_2, \bar{H}} &+ \frac{\partial n}{\partial \bar{H}} \Big|_{\bar{\theta}_2, t} \frac{\partial \bar{H}}{\partial t} \Big|_{\bar{\theta}_2, P_\theta} + \frac{\partial n}{\partial \bar{\theta}_2} \Big|_{\bar{H}, t} \frac{\partial \bar{H}}{\partial P_\theta} \Big|_{\bar{\theta}_2, t} \\ &= \frac{\partial \bar{H}}{\partial P_\theta} \Big|_{\bar{\theta}_2, t} \frac{\partial}{\partial \bar{H}} \left[-\dot{P}_\theta|_T n + \tilde{\mathcal{D}} \frac{\partial \bar{H}}{\partial P_\theta} \Big|_{\bar{\theta}_2, t} \frac{\partial n}{\partial \bar{H}} \Big|_{\bar{\theta}_2, t} \right]. \end{aligned} \quad (35)$$

To complete the description of the transport equation, the Hamiltonian $\bar{H}(\bar{\theta}_2, P_\theta, t)$ must be specified. Formally, the Hamiltonian is given by the expression

$$\bar{H} = e\phi^{(0)}[r(P_\theta)] + e\delta\phi[r(P_\theta), \bar{\theta}_2, t] - \frac{\omega_2 + \Delta\omega}{2}P_\theta, \quad (36)$$

where $\phi^{(0)}(r)$ is the unperturbed potential and $\delta\phi(r, \bar{\theta}, t)$ is the perturbation due to the mode.

From Eqs. (24) and (25) one can see that \dot{D}_2 and $\Delta\omega$ are explicitly first order in the small halo density n_h . In the experiments, n_h/n_c is of order 10^{-2} . Since we intend to calculate \dot{D}_2 and $\Delta\omega$ only to first order in n_h , the Hamiltonian for the evolution of $n_h(\bar{\theta}_2, P_\theta, t)$ need only be accurate to zero order in n_h . Thus, the contribution of the halo charge density to the two potentials in the Hamiltonian may be neglected. In the halo region, the two potentials then reduce to the form

$$\phi^{(0)}(r) \simeq -Ne \ln \left(\frac{r^2}{R_w^2} \right), \quad (37)$$

$$\begin{aligned} \delta\phi(r, \bar{\theta}_2, t) &\simeq \delta\phi_c(r, \bar{\theta}_2, t) \\ &= Ne \frac{R_c}{r^2} \left(1 - \frac{r^4}{R_w^4} \right) D_2(t) \cos 2\bar{\theta}_2. \end{aligned} \quad (38)$$

Note that both potentials vanish at the wall, where $r = R_w$. By using the replacement $P_\theta = eBr^2/2c$, the Hamiltonian takes the form

$$\bar{H} = -Ne^2 \ln \left(\frac{P_\theta}{P_w} \right) + Ne^2 \frac{P_c}{P_\theta} \left(1 - \frac{P_\theta^2}{P_w^2} \right) D_2(t) \cos 2\bar{\theta}_2 - \frac{\omega_2 + \Delta\omega}{2} P_\theta, \quad (39)$$

where $P_c = eBR_c^2/2c$ and $P_w = eBR_w^2/2c$ are simply constants. This Hamil-

tonian is used to obtain the numerical solution for the halo density in Section 6.

For the analytic results obtained in Sections 5 and 6, further simplification of the Hamiltonian is useful. In the resonant region, the Hamiltonian may be Taylor-expanded with respect to P_θ about the resonant value $P_\theta = P_r$, which is defined through the relation

$$\frac{\omega_2 + \Delta\omega}{2} = \frac{\partial}{\partial P_\theta} \left[-Ne^2 \ln \left(\frac{P_\theta}{P_w} \right) \right]_{P_\theta=P_r} = -\frac{Ne^2}{P_r}. \quad (40)$$

The resonant momentum can be rewritten as $P_r = P_2 + \Delta P(t)$, where $P_2 = -2Ne^2/\omega_2$ is the resonant momentum for the linear mode frequency and $\Delta P(t) \simeq 2Ne^2\Delta\omega(t)/\omega_2^2$ is a small correction due to the nonlinear frequency shift.

Taylor-expanding the first term in Hamiltonian (39) and using Eq. (40)

yields the result

$$-Ne^2 \ln \left(\frac{P_\theta}{P_w} \right) \simeq -Ne^2 \ln \left(\frac{P_r}{P_w} \right) + \left(\frac{\omega_2 + \Delta\omega}{2} \right) (P_\theta - P_r) + \frac{Ne^2}{2} \left(\frac{P_\theta - P_r}{P_r} \right)^2, \quad (41)$$

where higher than second order terms in $(P_\theta - P_r)/P_r$ have been neglected.

In Taylor-expanding the second term in Hamiltonian (39), we anticipate that D_2/R_c may be taken to be second order in $(P_\theta - P_r)/P_r$ in the resonant region, so the other factors may be evaluated in zeroth order, that is, P_θ may simply be replaced by $P_r = P_2$. By using the relation $P_c/P_r \simeq R_c^2/R_2^2 \simeq 1/2$ and by neglecting the quantity P_r^2/P_w^2 compared to unity, the second term may be approximated by the expression $(Ne^2/2)(D_2/R_c) \cos 2\bar{\theta}_2$.

Combining these results yields the simplified Hamiltonian

$$\bar{H} = \frac{Ne^2}{2} \left[\left(\frac{P_\theta - P_r}{P_r} \right)^2 + \frac{D_2}{R_c} \cos 2\bar{\theta}_2 \right], \quad (42)$$

where purely time-dependent terms have been dropped since such terms do not enter Hamilton's equations of motion. In using this Hamiltonian, we

must remember that P_r and D_2 have explicit time-dependence.

4 Damping coefficient and nonlinear frequency shift under the assumptions used in the previous heuristic treatment

The purpose of this section is to recover the damping rate obtained in the previous heuristic treatment.^{15,20} We also will obtain the corresponding nonlinear frequency shift.

The heuristic treatment assumes a top hat core, so the Green's function integrals for $\dot{D}_2(t)$ and $\dot{\alpha}_2(t) = \Delta\omega(t)$ are those given in Eqs. (24) and (25), and the Hamiltonian is that given in Eq. (42).

The evolution of the halo takes place in two stages: In the first stage, the halo expands radially until it reaches the wall. At the wall, halo particles are absorbed continuously and a quasi-steady state density distribution is established. The heuristic treatment attempts to calculate the damping rate and nonlinear frequency shift for this quasi-steady state.

The heuristic treatment neglects the explicit time dependence in the Hamil-

tonian, that is, in $D_2(t)$ and $P_r(t)$. As was discussed in the introduction, neglecting this time dependence is a mistake, since the theory then misses the feedback mechanism that maintains the constant damping rate.

Finally, the heuristic treatment neglects diffusion and treats the coefficient of mobility as constant in the halo region. From Eq. (30) one can see that the constancy of μ and of $r\partial\phi^{(0)}/\partial r$ in the halo region implies the constancy of $\dot{P}_\theta|_T$ in the halo region.

Setting $\partial n/\partial t$, $\partial \bar{H}/\partial t$ and \mathcal{D} equal to zero and using the constancy of $\dot{P}_\theta|_T$ in Eq. (35) yields the simple steady state transport equation

$$\frac{\partial n}{\partial \bar{\theta}_2} + \dot{P}_\theta|_T \frac{\partial n}{\partial \bar{H}} = 0, \quad (43)$$

with the solution

$$n(\bar{\theta}_2, \bar{H}) = n(\bar{H} - \bar{\theta}_2 \dot{P}_\theta|_T). \quad (44)$$

This result is easy to understand physically. For constant $\dot{P}_\theta|_T$, the mobility flow is incompressible and can be incorporated along with the incompressible

$\mathbf{E} \times \mathbf{B}$ -drift flow in a combined Hamiltonian

$$\bar{K} = \bar{H}(\bar{\theta}_2, P_\theta) - \bar{\theta}_2 \dot{P}_\theta|_T. \quad (45)$$

Moreover this combined Hamiltonian has no explicit time dependence and so is a constant of the motion. The density flows incompressibly along curves of constant \bar{K} .

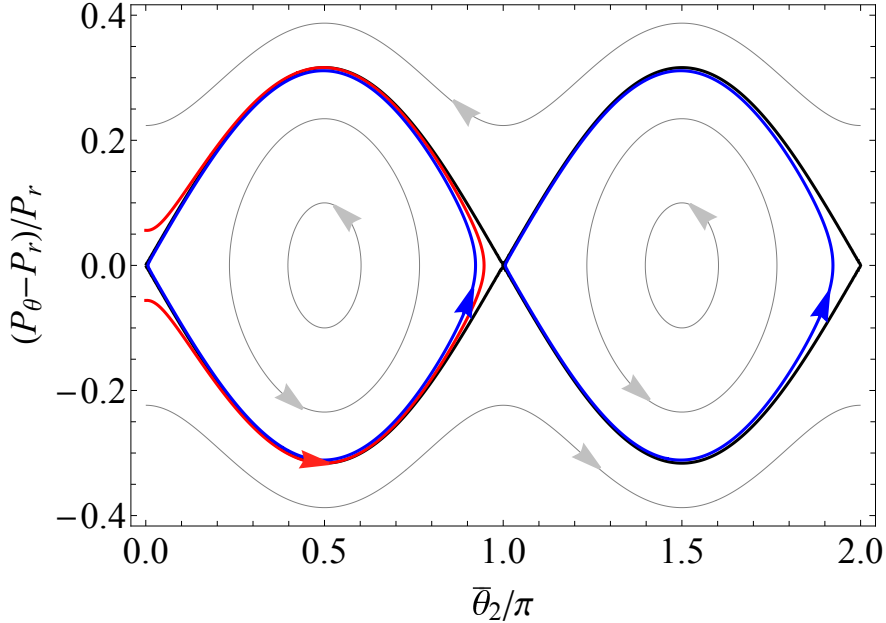


Figure 2: Selected curves of constant \bar{H} (in gray) and of constant \bar{K} (in red) in the resonant region of the phase space. Blue curves are of critical $\bar{K} = \bar{K}_c$.

Fig. (2) shows selected curves of constant \bar{H} and of constant \bar{K} in the resonant region of the phase space, $[\bar{\theta}_2, (P_\theta - P_r)/P_r]$. This figure reproduces the

resonant region of Fig. (1b), but using the rectangular phase space coordinates $[\bar{\theta}_2, (P_\theta - P_r)/P_r]$ rather than the polar configuration coordinates $(r, \bar{\theta}_2)$.

The gray curves in Fig. (2) are contours of constant \bar{H} and corresponds to the gray curves of Fig. (1b), which there were called eqipotential contours in the wave frame. Of course, \bar{H} is equal to the wave frame potential up to a multiplicative constant, e .

The graphs are drawn for the characteristic value $D_2/R_c = 0.05$ and the unrealistically large value $\dot{P}_\theta|_T/Ne^2 = 2 \times 10^{-3}$. This large value is used to make the distinction between curves of constant \bar{H} and curves of constant $\bar{K} = \bar{H} - \bar{\theta}_2 \dot{P}_\theta|_T$ visible; in the experiments, $\dot{P}_\theta|_T$ has a value of order $\dot{P}_\theta|_T \sim 10^{-5}$.

In the absence of transport, halo particles would flow along curves of constant \bar{H} , and the arrows show the direction of the flow [i.e., $\dot{\bar{\theta}}_2 = \partial \bar{H} / \partial P_\theta$].

Recall here that P_θ and P_r are negative for negatively charged particles.

There are open contours extending from $\bar{\theta}_2 = 0$ to $\bar{\theta}_2 = 2\pi$, closed cat's eye

contours and a separatrix between the two (shown as a thick grey contour).

On the separatrix, \bar{H} has the value $\bar{H}_S = (Ne^2/2)(D_2/R_c)$, on the open

contours $\bar{H} > \bar{H}_S$ and on the closed cat's eye contours $\bar{H} < \bar{H}_S$.

By solving Eq. (42) for $(P_\theta - P_r)/P_r$, one obtains the relation

$$\frac{P_\theta - P_r}{P_r} = \pm \sqrt{\frac{2\bar{H}}{Ne^2} - \frac{D_2}{R_c} \cos 2\bar{\theta}_2}, \quad (46)$$

where the plus sign applies in the upper half of Fig. (2) and the minus sign

in the lower half. At the separatrix $\bar{H} = (Ne^2/2)(D_2/R_c)$, Eq. (46) reduces

to the simple result

$$\frac{P_\theta - P_r}{P_r} = \pm \sqrt{\frac{2D_2}{R_c} |\sin \bar{\theta}_2|}, \quad (47)$$

where use has been made of the relation $1 - \cos 2\bar{\theta}_2 = 2 \sin^2 \bar{\theta}_2$. In Eq. (47) the

quantity $P_\theta^+(\bar{\theta}_2)$ is the locus of points along the top portion of the separatrix

and $P_\theta^-(\bar{\theta}_2)$ is the locus along the bottom portion.

The red curves in Fig. (2) corresponds to the red curve in Fig. (1b). These

are curves are trajectories of constant \bar{K} , specifically $\bar{K} = \bar{H}_s - (\pi/2)\dot{P}_\theta|_T$.

A particle on this trajectory enters the cats-eye region from below, that is, crosses the separatrix $\bar{H} = \bar{H}_s$ from below, at the angle $\bar{\theta}_2 = \pi/2$, sweeps around half of the cats-eye and exits to the region above again at the angle $\bar{\theta}_2 = \pi/2$.

The two blue curves in Fig. (2) were not shown in Fig. (1b). These curves are critical trajectories of constant \bar{K} . The critical trajectory on the left has the value $\bar{K}_c = \bar{H}_s$. A particle on this trajectory enters the cats-eye region from below at $\bar{\theta}_2$ just to the right of $\bar{\theta}_2 = 0$, sweeps around the cats-eye and exits to the region above at the same angle at which it entered the cat's-eye region. The second critical trajectory is identical except that it is displaced to the right by $\Delta\bar{\theta}_2 = \pi$ and has the value $\bar{K}'_c = \bar{H}_s - \pi\dot{P}_\theta|_T$. All of the constant \bar{K} trajectories inside the blue curves are closed trajectories, and all of the constant \bar{K} trajectories outside are open trajectories.

Since the halo particles cannot access the closed trajectories, the density inside the region bounded by the blue curves (i.e., $\bar{K} < \bar{K}_c$) remains zero.

The open trajectories outside the region bounded by the blue curves (i.e., $\bar{K} > \bar{K}_c$) all wind down to the lower edge of the halo region, just outside the core, where the halo density has the same value n_h . Since the flow is incompressible, the density must have the constant value everywhere in the halo outside the blue curves.

Thus, in the region $0 < \bar{\theta}_2 < \pi$, the halo density is given by the simple expression

$$n_h(\bar{\theta}_2, P_\theta) = n_h \Theta[\bar{K}(\bar{\theta}_2, P_\theta) - \bar{H}_s], \quad (48)$$

where $\Theta(x)$ is a step-function. Since the halo density is periodic in $\bar{\theta}_2$ with period π , we will only need the density in the range $0 < \bar{\theta}_2 < \pi$. Because of this periodicity, we only need expression (48). Using the smallness of $\dot{P}_\theta|_T$ and the definition $\bar{K} = \bar{H}(\bar{\theta}_2, P_\theta) - \bar{\theta}_2 \dot{P}_\theta|_T$, we Taylor-expand the Theta function obtaining the result

$$n_h(\bar{\theta}_2, P_\theta) = n_h \Theta[\bar{H}(\bar{\theta}_2, P_\theta) - \bar{H}_s] - \dot{P}_\theta|_T \bar{\theta}_2 n_h \delta[\bar{H}(\bar{\theta}_2, P_\theta) - \bar{H}_s], \quad (49)$$

where the delta function in the second term comes from the derivative of the step function. The first term in this expression represents the density below and above the cat's-eye region, and the second term represents the density in the thin ribbon of particles being swept around the interior edge of the cat's-eye region, that is the thin ribbon between the thick gray curve and the blue curve in Fig (2). In this description, the density above the cat's-eye region also has uniform density n_h , but we will see later that this is not the case when the explicit time-dependence in D_2 and P_r is taken into consideration.

We will denote the thickness of the ribbon along the upper portion of the separatrix by $\Delta\bar{H}^+(\bar{\theta}_2)$ and the thickness along the lower portion by $\Delta\bar{H}^-(\bar{\theta}_2)$. Here, the usage of the + and - signs is the same as that in Eq. (47). In this section, both $\Delta\bar{H}^+(\bar{\theta}_2)$ and $\Delta\bar{H}^-(\bar{\theta}_2)$ are equal to $-\dot{P}_\theta|_T \bar{\theta}_2$, but in the next section, we will find that the explicit time dependence makes $\Delta\bar{H}^+(\bar{\theta}_2)$ and $\Delta\bar{H}^-(\bar{\theta}_2)$ unequal, so it is useful to allow for this possibility at the outset

rewriting Eq. (49) as

$$n_h(\bar{\theta}_2, P_\theta) = n_h \Theta[\bar{H}(\bar{\theta}_2, P_\theta) - \bar{H}_s] + \Delta \bar{H}^\pm(\bar{\theta}_2) n_h \delta[\bar{H}(\bar{\theta}_2, P_\theta) - \bar{H}_s]. \quad (50)$$

Returning to Eqs. (24) and (25) for the damping rate and frequency shift, note that the $\bar{\theta}_2$ -integrals are periodic with period π , so the range of integration can be reduced to $\bar{\theta}_2 = 0$ and $\bar{\theta}_2 = \pi$ by introducing a factor of 2. Within this range of integration, $\sin 2\bar{\theta}_2$ is odd about $\bar{\theta}_2 = \pi/2$. Since Hamiltonian (42) is even about $\bar{\theta}_2 = \pi/2$, the first term in Eq. (50) does not contribute to the integral for the damping rate. Substituting the second term, neglecting R_2^4/R_w^4 compared to unity, setting $dP_\theta = (eB/c)r'dr'$ and approximating $P_\theta \simeq P_r$ when P_θ is explicitly expressed in the integrand yields the expression

$$\frac{dD_2}{dt} = -\left(\frac{2ecR_c}{B}\right) \int_0^\pi d\bar{\theta}_2 \int_{P_c}^{P_w} \frac{dP_\theta}{P_r} \Delta \bar{H}^\pm(\bar{\theta}_2) n_h \delta[\bar{H}(\bar{\theta}_2, P_\theta) - \bar{H}_s] \sin 2\bar{\theta}_2. \quad (51)$$

Note here that both dP_θ and P_θ are negative. The argument of the delta function vanishes at the two values $P_\theta^\pm(\bar{\theta}_2)$ given by Eq. (47), so Eq. (51)

reduces to the form

$$\dot{D}_2(t) = -\left(\frac{2ecn_hR_c}{B}\right) \sum_{\pm} \int_0^\pi d\bar{\theta}_2 \frac{\Delta\bar{H}(\bar{\theta}_2) \sin 2\bar{\theta}_2}{-P_\theta^\pm(\bar{\theta}_2) |\partial\bar{H}/\partial P_\theta|_{P_\theta^\pm}}. \quad (52)$$

From Hamiltonian (42) and Eq. (47) one obtains the relation

$$-P_r \left| \frac{\partial\bar{H}}{\partial P_\theta} \right|_{P_\theta^\pm} = Ne^2 \sqrt{\frac{2D_2}{R_c}} |\sin \bar{\theta}_2|, \quad (53)$$

and substituting into Eq. (52) then yields the equation

$$\dot{D}_2(t) = -\left(\frac{4cn_hR_c}{eBN}\right) \sqrt{\frac{R_c}{2D_2}} \sum_{\pm} \int_0^\pi d\bar{\theta}_2 \Delta\bar{H}^\pm(\bar{\theta}_2) \cos \bar{\theta}_2, \quad (54)$$

where use has been made of the double angle formula, $\sin 2\bar{\theta}_2 = 2 \sin \bar{\theta}_2 \cos \bar{\theta}_2$,

and $P_\theta^\pm(\bar{\theta}_2) - P_r$, which is higher order in D_2/R_c , has been neglected. For

the present case, where $\Delta\bar{H}^\pm(\bar{\theta}_2) = -\dot{P}_\theta|_T \bar{\theta}_2$, the sum over + and - simply

introduces a factor of 2, and Eq. (54) reduces to the result

$$\begin{aligned} \dot{D}_2(t) &= \left(\frac{4n_h c R_c \dot{P}_\theta|_T}{BN e}\right) \sqrt{\frac{R_c}{2D_2}} \int_0^\pi d\bar{\theta}_2 \bar{\theta}_2 \cos \bar{\theta}_2 \\ &= -\left(\frac{16n_h c R_c \dot{P}_\theta|_T}{BN e}\right) \sqrt{\frac{R_c}{2D_2}}. \end{aligned} \quad (55)$$

By using the relation $|dN/dt| = 2\pi(cn_h/eB)\dot{P}_\theta|_T$, Eq. (55) yields the result

$$\dot{D}_2(t) = -\frac{4}{\pi} \sqrt{\frac{2R_c}{D_2}} \frac{R_c}{N} \left| \frac{dN}{dt} \right|, \quad (56)$$

which is identical to that given in Eq. (10) for the earlier heuristic treatment.

Since the damping rate comes exclusively from the second term in Eq. (49)

and since this term represents particles being swept around the cats-eyes the

damping comes exclusively from particles being swept around the cats-eyes,

as was assumed in the heuristic treatment.

Since the heuristic treatment used angular momentum balance, omitting

the torque exerted by the transport, we must ask why the two treatments

yield the same damping rate. The answer is that a particle is swept around

the cats-eye orbit very rapidly, and the torque induced change in angular

momentum during this short period is small compared to the wave induced

change in angular momentum. Both treatments are accurate only to the first

order in the small quantity $\dot{P}_\theta|_T$; in higher order they would differ.

From the even and odd arguments given earlier, one can see that the first term in Eq. (49) does contribute to the integral for the frequency shift in Eq. (25). In this case, the contribution from the second term may be neglected compared to that from the first because of the smallness of $\dot{P}_\theta|_T$. Substituting the first term, neglecting R_2^4/R_w^4 compared to unity, setting $dP_\theta = (eB/c)r'dr'$ and approximating $P_\theta \simeq P_r$ when P_θ is explicitly expressed in the integrand yields the expression

$$D_2\Delta\omega = \left(\frac{2ecR_c}{B}\right) \int_0^\pi d\bar{\theta}_2 \int_{P_c}^{P_w} \frac{dP_\theta}{P_r} n_h \Theta[\bar{H}(\bar{\theta}_2, P_\theta) - \bar{H}_s] \cos 2\bar{\theta}_2 \quad (57)$$

The contribution from the third term in Eq. (49) has been neglected compared to that from the first two terms because of the small factor $\dot{P}_\theta|_T$. In the integrand of the first term, the factor $\Theta[\bar{H}(\bar{\theta}_2, P_\theta) - \bar{H}_s]$ can be replaced by $\Theta[\bar{H}(\bar{\theta}_2, P_\theta) - \bar{H}_s] - 1$, since the term -1 is killed by the integral over $\cos 2\bar{\theta}_2$. The quantity $\Theta[\bar{H}(\bar{\theta}_2, P_\theta) - \bar{H}_s]$ has the value -1 inside the cat's-eye region and zero everywhere else. By using Eq. (47), the integral over the cat's-eye

region can be evaluated yielding the result

$$D_2\Delta\omega = \left(\frac{2ecn_hR_c}{B}\right) \int_0^\pi d\bar{\theta}_2 2\sqrt{\frac{2D_2}{R_c}} |\sin \bar{\theta}_2| \cos 2\bar{\theta}_2 = \left(\frac{-8ecn_hR_c}{3B}\right) \sqrt{\frac{2D_2}{R_c}}.$$
(58)

Thus far, we have determined two contributions to the frequency: ω_2 as given by Eq. (20) and $\Delta\omega$ given here. The contribution ω_2 arises from the linear density perturbation at the surface of the core, and the nonlinear frequency shift $\Delta\omega$ arises from the density void in the cat's-eye region. Of course, $\Delta\omega$ is first order in the small quantity n_h , but also ω_2 contains a term of order n_h , since the fall off in density at the surface of the core is $n_c - n_h$, not simply n_c . Thus, one cannot think of $\Delta\omega$ as the only order n_h correction to the frequency, that is, the correction relative to the frequency in the absence of a halo. Rather, $\Delta\omega$ is a nonlinear frequency shift that arises when the radially expanding halo passes the resonant region leaving a plasma void in the cat's-eye regions. There also is a density gradient at the leading edge of the expanding halo, and the mode potential acting on

this gradient produces another frequency correction of n_h . However, for the steady state halo density profile envisioned in this section, where the halo has reached the wall, this latter density gradient appears very near the wall, where the mode potential approaches zero. That is, this last correction should be negligibly small for the steady state profile. The first term is the nonlinear frequency shift arising from the integral over the cats-eye region. The second term, which is proportional to D_2 , is a linear correction to the frequency [i.e., $\delta\omega = -2\pi ecn_h^{(0)}/B]$, arising from the perturbed charge density at the lower edge of the halo .

5 Perturbative solution including the explicit time-dependence in the Hamiltonian

In this section, we construct a perturbative solution for the halo density that includes the effect of the explicit time dependence in the Hamiltonian. The calculation focuses on the thin ribbon of particles being swept around the cats-eye region and yields a more accurate expression for the thickness of the ribbon $\Delta\bar{H}^\pm(\bar{\theta}_2)$. We continue to neglect diffusion and treat $\dot{P}_\theta|_T$ as a constant.

Transport equation (35) then reduces to the form

$$\left(\frac{\partial n}{\partial t}\right)_{\bar{\theta}_2, \bar{H}} + \left(\frac{\partial n}{\partial \bar{H}}\right)_{\bar{\theta}_2, t} \left(\frac{\partial \bar{H}}{\partial t}\right)_{\bar{\theta}_2, P_\theta} + \left(\frac{\partial n}{\partial \bar{\theta}_2}\right)_{\bar{H}, t} \left(\frac{\partial \bar{H}}{\partial P_\theta}\right)_{\bar{\theta}_2, t} + \dot{P}_\theta|_T \left(\frac{\partial n}{\partial \bar{H}}\right)_{\bar{\theta}_2, t} \left(\frac{\partial \bar{H}}{\partial P_\theta}\right)_{\bar{\theta}_2, t} = 0. \quad (59)$$

Both of the time derivatives are first order small in $\dot{P}_\theta|_T$, and the last term is first order small in $\dot{P}_\theta|_T$. Thus, we construct a perturbation solution for the halo density, expanding in the smallness of $\dot{P}_\theta|_T$. Writing the density as

$n = n^{(0)} + n^{(1)} + \dots$, where $n^{(1)}/n^{(0)}$ is of order of $\dot{P}_\theta|_T$, yields the zeroth order transport equation

$$\left(\frac{\partial n^{(0)}}{\partial \bar{\theta}_2} \right)_{\bar{H},t} \left(\frac{\partial \bar{H}}{\partial P_\theta} \right)_{\bar{\theta}_2,t} = 0, \quad (60)$$

with the solution

$$n^{(0)} = n^{(0)}(\bar{H}, t) = n_h \Theta[\bar{H}(\bar{\theta}_2, P_\theta, t) - \bar{H}_s]. \quad (61)$$

Of course, the zeroth order solution must agree with the first term in Eq. (49).

To the first order, the transport equation reduces to the form

$$\left(\frac{\partial n^{(1)}}{\partial \bar{\theta}_2} \right)_{\bar{H},t} + \left[\dot{P}_\theta|_T - \left(\frac{\partial P_\theta}{\partial t} \right)_{\bar{H}-\bar{H}_s, \bar{\theta}_2} \right] n_h \delta[\bar{H} - \bar{H}_s] = 0, \quad (62)$$

where

$$\left(\frac{\partial P_\theta}{\partial t} \right)_{\bar{H}-\bar{H}_s, \bar{\theta}_2} = - \frac{[\partial(\bar{H} - \bar{H}_s)/\partial t]_{\bar{\theta}_2, P_\theta}}{[\partial(\bar{H} - \bar{H}_s)/\partial P_\theta]_{\bar{\theta}_2, t}} \quad (63)$$

is a standard relation for partial derivatives. In the denominator of the Right Hand Side, use has been made of the fact that $\bar{H}_s = \bar{H}_s(t)$ is independent of P_θ .

The time derivative on the Left Hand Side of Eq. (63) is to be carried out holding $\bar{\theta}_2$ and $\bar{H} - \bar{H}_s$ constant, and the delta function in Eq. (62) further requires that $\bar{H} - \bar{H}_s = 0$. The solution for $P_\theta = P_\theta(\bar{H} - \bar{H}_s, \bar{\theta}_2, t)$ is given by Eq. (46), so we obtain the time derivative

$$\left(\frac{\partial P_\theta^\pm}{\partial t} \right)_{\bar{H} - \bar{H}_s, \bar{\theta}_2} = \frac{\partial P_r}{\partial t} \left[1 \pm \sqrt{\frac{2D_2}{R_c}} \sin \bar{\theta}_2 \right] \pm \sqrt{\frac{2D_2}{R_c}} \frac{\dot{D}_2}{2D_2} P_r \sin \bar{\theta}_2. \quad (64)$$

By using the relation

$$\frac{1}{P_r} \frac{\partial P_r}{\partial t} = -\frac{1}{\omega_2} \frac{\partial \Delta\omega}{\partial t} \quad (65)$$

and Eq. (58), and keeping only to the leading term, Eq. (64) reduces to the form

$$\frac{\partial P_\theta^\pm}{\partial t} = \pm P_r \frac{\dot{D}_2}{2D_2} \sqrt{\frac{2D_2}{R_c}} \sin \bar{\theta}_2. \quad (66)$$

Motivated by Eq. (49), we guess the form

$$n^{(1)}(\bar{\theta}_2, \bar{H}) = \Delta \bar{H}^\pm(\bar{\theta}_2) n_h \delta(\bar{H} - \bar{H}_s) \quad (67)$$

and see that transport equation (62) is satisfied if $\Delta \bar{H}^\pm(\bar{\theta}_2)$ satisfies the

differential equation

$$\frac{\partial \Delta \bar{H}^\pm}{\partial \bar{\theta}_2} = \frac{\partial P_\theta^\pm}{\partial t} - \dot{P}_\theta|_T. \quad (68)$$

Physically, this result is exactly what one expects for the simple feedback mechanism described in the introduction. Particles cross the separatrix and join the thin ribbon of particles being swept around the cat's-eye region at a rate determined by the mobility flux measured relative to the moving separatrix.

By definition, the critical contour defining the edge of the thin ribbon of particles being swept around the cat's-eye region (see the blue curve in Fig. (2)) crosses the separatrix and enters the cat's-eye region at the angle $\bar{\theta}_2 = 0$. Thus, we take $\Delta \bar{H}^-(\bar{\theta}_2 = 0)$ to have the value zero and integrate Eq. (68) to obtain the thickness along the lower separatrix

$$\begin{aligned} \Delta \bar{H}^-(\bar{\theta}_2) &= \int_0^{\bar{\theta}_2} d\bar{\theta}_2 \left(\frac{\partial P_\theta^-}{\partial t} - \dot{P}_\theta|_T \right) \\ &= -\bar{\theta}_2 \dot{P}_\theta|_T - P_r \frac{\dot{D}_2}{2D_2} \sqrt{\frac{2D_2}{R_c}} (1 - \cos \bar{\theta}_2). \end{aligned} \quad (69)$$

We assume continuity of the thickness at $\bar{\theta}_2 = \pi$, taking $\Delta\bar{H}^+(\pi) = \Delta\bar{H}^-(\pi)$,

and obtaining the thickness along the upper separatrix

$$\begin{aligned}\Delta\bar{H}^+(\bar{\theta}_2) &= \Delta\bar{H}^+(\pi) + \int_{\pi}^{\bar{\theta}_2} d\bar{\theta}_2 \left(\frac{\partial P_\theta^+}{\partial t} - \dot{P}_\theta|_T \right) \\ &= -\bar{\theta}_2 \dot{P}_\theta|_T - P_r \frac{\dot{D}_2}{2D_2} \sqrt{\frac{2D_2}{R_c}} (3 + \cos \bar{\theta}_2).\end{aligned}\quad (70)$$

Because $\partial P_\theta^+/\partial t$ and $\partial P_\theta^-/\partial t$ are not equal, $\Delta\bar{H}^+(\bar{\theta}_2)$ and $\Delta\bar{H}^-(\bar{\theta}_2)$ are not equal. Significantly, $\Delta\bar{H}^+(\bar{\theta}_2)$ goes to zero for a value of $\bar{\theta}_2$ that is greater than zero. At this value of $\bar{\theta}_2$, which we call $\bar{\theta}_{\text{out}}$, the critical contour passes through the upper separatrix to the region above the trapped particle orbits.

Requiring $\Delta\bar{H}^+(\bar{\theta}_{\text{out}})$ to be zero, setting $\dot{P}_\theta|_T = (eB/c)(|\dot{N}|/2\pi n_h)$ and $P_r = (eB/c)R_c^2$ in Eq. (70) yields the relation

$$0 = \bar{\theta}_{\text{out}} \frac{|\dot{N}|}{N} + \frac{n_h}{n_c} \frac{\dot{D}_2}{D_2} \sqrt{\frac{2D_2}{R_c}} (3 + \cos \bar{\theta}_{\text{out}}). \quad (71)$$

In Section IV, Eq. (54) for the damping rate was rewritten in a form that allows for the possibility that $\Delta\bar{H}^+(\bar{\theta}_2) \neq \Delta\bar{H}^-(\bar{\theta}_2)$. Integrating Eq. (54) by

parts yields the expression

$$\dot{D}_2 = \frac{4n_h R_c c}{NeB} \sqrt{\frac{R_c}{2D_2}} \sum_{+,-} \int_0^\pi d\bar{\theta}_2 \sin \bar{\theta}_2 \frac{\partial \Delta \bar{H}^\pm(\bar{\theta}_2)}{\partial \bar{\theta}_2}. \quad (72)$$

Here the integral along the lower separatrix, corresponding to the minus sign

in $\Delta \bar{H}^\pm(\bar{\theta}_2)$, extends from $\bar{\theta}_2 = 0$ to $\bar{\theta}_2 = \pi$, and the integral along the upper separatrix, corresponding to the plus sign, extends only from $\bar{\theta}_{\text{out}}$ to π .

Performing the integrations and again substituting $\dot{P}_\theta|_T = (eB/c)(|\dot{N}|/2\pi n_h)$

and $P_r = (eB/c)R_c^2$ yields the result

$$\dot{D}_2 = -\frac{R_c}{\pi} \sqrt{\frac{2R_c}{D_2}} \left[\frac{|\dot{N}|}{N} (3 + \cos \bar{\theta}_{\text{out}}) + \frac{n_h \dot{D}_2}{n_c D_2} \sqrt{\frac{D_2}{2R_c}} \left(\bar{\theta}_{\text{out}} - \frac{\sin 2\bar{\theta}_{\text{out}}}{2} \right) \right]. \quad (73)$$

As a simple check on this result, note that when \dot{D}_2 and $\bar{\theta}_{\text{out}}$ are arbitrarily set equal to zero on the Right Hand Side, the damping rate in Eq. (56) is recovered. Also, when \dot{D}_2 on the Right Hand Side is made negative, the new terms have the effect of reducing the damping rate, as expected from the simple feedback hypothesis proposed in the introduction.

However, there is a caveat associated with the use of Eq. (54). This inte-

gral expression for the damping rate only includes the contribution from the thin ribbon of particles being swept around the inside edge of the trapped particle region. In Section 4 we argued that the density in the region below and above the trapped particle separatrix is uniform, and hence the contribution from these regions to the damping rate is zero. A Hamiltonian flow is incompressible, but there can be region of void (i.e. zero density) intermixed with region of finite, uniform density. We will see from the numerical solution in Section 6 that when the explicit time dependence is retained in the Hamiltonian, the region above the separatrix does develop a complex structure of void and finite density layers. A small amount of diffusion does smooth out this complex structure, but we must verify from the numerical solution that the contribution to the damping from this region is negligible.

Recall that the frequency shift was written in Section 4 as an integral over the void associated with the trapped particle region. Since a modification of the thin ribbon of particles being swept around the lower edge of the

trapped particle region makes negligible change in the value of this integral, the expression for the frequency shift is not significantly changed.

Returning to Eq. (73) for the damping rate, we collect all terms proportional to \dot{D}_2 on the Left Hand Side and divide by the coefficient of \dot{D}_2 obtaining

$$\dot{D}_2 = -\frac{R_c \sqrt{\frac{2R_c}{D_2} \frac{|\dot{N}|}{N}} \left(3 + \cos \bar{\theta}_{\text{out}} \right)}{\pi + \frac{n_h R_c}{n_c D_2} \left(\bar{\theta}_{\text{out}} - \frac{\sin 2\bar{\theta}_{\text{out}}}{2} \right)} \quad (74)$$

This equation must be solved in conjunction with Eq. (71). Taking the dependent variable to be the scaled displacement D_2/R_c and scaling time as $t|\dot{N}|/N$ leaves only the single parameter n_h/n_c in Eqs. (71) and (72). In all the experiments, this parameter has the approximate value $n_h/n_c \simeq 10^{-2}$.

Taking this value and integrating Eqs. (74) and (71) numerically yields the dashed blue curve in Fig. (3). The solid curve is the analytic solution in Eq. (11). We can see that the correct damping rate is nearly constant throughout the course of damping, instead of steeping at low mode amplitudes as in the original solution. The correction solution captures the feedback mechanism

postulated in Section 1.

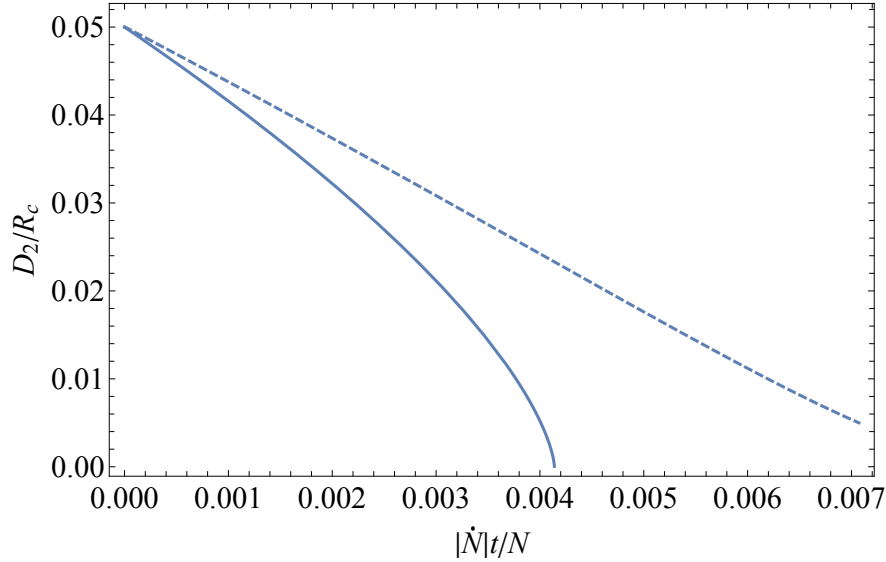


Figure 3: Plots of D_2/R_c vs t . The solid curve is the original solution in Eq. (11), the blue dashed curve is the corrected solution.

Before moving on to a re-examination of the nonlinear frequency shift, we anticipate a result from the numerical solution in Section 6. The halo density above the cat's-eye region turns out to have a lower average density than that below the cat's-eye region. For the case where the flow is Hamiltonian, this sounds impossible, since a Hamiltonian flow is incompressible. However, there can be regions of void mixed in with regions of finite uniform density, and we well see from the numerical solution that when the explicit time-dependence

is retained in the Hamiltonian, the flow above the cat's-eye region develops a complex, interlaced structure of void and finite density layers. To see these interlaced layers, the reader may wish to skip ahead to Fig. (6) in Section 6. Including a small amount of diffusion in the transport equation smooths out this layer structure yielding a smooth density n'_h , where n'_h is smaller than the density below the cat's-eye region, n_h .

To determine the density n'_h , we first recall from Eq. (68) that the rate at which halo particles enter the cat's-eye region from below, joining the thin ribbon of particles being swept around the edge of the cat's-eye region, is the expression

$$(\text{rate})^- = n_h \left(\frac{c}{eB} \right) \int_0^\pi d\bar{\theta}_2 \left(\dot{P}_\theta|_T - \frac{\partial P_\theta^-}{\partial t} \right). \quad (75)$$

Likewise the rate at which the halo particles move away from the cat's-eye to the region above is the expression

$$(\text{rate})^+ = n'_h \left(\frac{c}{eB} \right) \int_0^\pi d\bar{\theta}_2 \left(\dot{P}_\theta|_T - \frac{\partial P_\theta^+}{\partial t} \right). \quad (76)$$

Since all of the particles that enter through the lower separatrix are rapidly swept out through the upper separatrix, the two rates must be nearly equal, yielding the relation

$$\frac{n'_h}{n_h} = \frac{\dot{P}_\theta|_T \pi + P_r \dot{D}_2 \sqrt{2/R_c D_2}}{\dot{P}_\theta|_T \pi - P_r \dot{D}_2 \sqrt{2/R_c D_2}}, \quad (77)$$

where use has been made of Eq. (47). For mode damping when \dot{D}_2 is negative, one can see that n'_h/n_h is smaller than unity. Comparing to the numerical results in Section 6, for scaled mode amplitude $D_2/R_c = 0.04$, n'_h/n_h has the value 0.58 in the numerical solution and the value 0.59 in Eq. (77), and for scaled amplitude $D_2/R_c = 0.03$, the corresponding numbers are 0.55 in simulation and 0.57 in Eq. (77).

Another halo feature that we expect to be different in the time-dependent case is that the leading edge is close to the outer separatrix but far from the trap wall, as we will see in Section 6. Since the halo leading edge surface is the angle-averaged trajectory of a particle at the leading edge, propagated outward by the influence of mobility, we assign a leading-edge Hamiltonian

$\bar{H}_l = \bar{H}_s$ when the mode damping starts, and estimate its time-dependence by integrating numerically

$$\frac{d\bar{H}_l}{dt} = \int_0^\pi \frac{d\bar{\theta}_2}{\pi} \frac{\partial \bar{H}}{\partial P_\theta} \dot{P}_\theta|_T, \quad (78)$$

with \bar{H} taking the approximated form (41). Beyond the outer separatrix, the time-dependent halo density is now approximated by

$$n^{(0)} = n'_h \Theta(\bar{H} - \bar{H}_s) \Theta(\bar{H}_l - \bar{H}). \quad (79)$$

To modify the expected frequency shift, we have to break up the integral in Eq. (57) into two parts, for $P_\theta < P_r$ and $P_\theta > P_r$, and for the $P_\theta > P_r$ part, we replace $n_h \Theta(\bar{H} - \bar{H}_s)$ with the expression in Eq. (79). The time-dependent frequency shift is modified to be

$$\Delta\omega^{(1)} = \Delta\omega^{(0)} \cdot \frac{1}{2} \left[1 + \frac{n'_h}{n_h} \left(1 + \frac{3}{2\sqrt{2}} \int_0^\pi d\bar{\theta}_2 \cos 2\bar{\theta}_2 \sqrt{\frac{2\bar{H}_l R_c}{Ne^2 D_2} - \cos 2\bar{\theta}_2} \right) \right], \quad (80)$$

where $\Delta\omega^{(0)}$ is the time-independent frequency shift in Eq. (58).

6 Numerical solution

In this section, the evolution of the halo density is followed numerically, including the effects of nonlinear $\mathbf{E} \times \mathbf{B}$ -drift orbits, mobility and diffusion. The perturbation on the core continues to be treated linearly, so the mode damping rate and frequency shift continue to be determined by Eqs. (24) and (25).

The halo density distribution evolves according to transport equation (29), with the Hamiltonian given by Eq. (39). This Hamiltonian is not simplified by Taylor expansion in P_θ about the resonant radius. We continue to take $\dot{P}_\theta|_T$ to be independent of P_θ and to relate the value of $\tilde{\mathcal{D}}$ to that of $\dot{P}_\theta|_T$ through the Einstein relation in Eq. (31).

To facilitate the numerical analysis, we write all quantities in dimensionless form, scaling energies by Ne^2 , angular momentum by $|P_c| = |eBR_c^2/2c|$ and lengths by R_c . This scaling is equivalent to choosing Ne^2 as the unit of

energy, $|P_c|$ as the unit of angular momentum, and R_c as the unit of length.

These choices imply that the unit of frequency is $Ne^2/|P_c| = |\omega_E(R_c)|$, or equivalently, that time is scaled by $1/|\omega_E(R_c)|$. Thus, we introduce the scaled quantities

$$p = \frac{P_\theta}{|P_c|}, \dot{p}|_T = \frac{\dot{P}_\theta|_T}{Ne^2}, D' = p\dot{p}|_T \left(\frac{T}{Ne^2} \right), t' = t|\omega_E(R_c)|. \quad (81)$$

The Hamiltonian then takes the form

$$\begin{aligned} h &\equiv \frac{\bar{H}}{Ne^2} \\ &= -\ln p + \frac{1}{p} \left[1 - \left(\frac{R_c}{R_w} \right)^4 p^2 \right] \frac{D_2}{R_c} \cos 2\bar{\theta} - \frac{p}{2} \left[-\frac{e}{|e|} \left(1 + \frac{R_c^4}{R_w^4} \right) + \frac{\Delta\omega}{|\omega_E(R_c)|} \right], \end{aligned} \quad (82)$$

where a constant term has been dropped, Eq. (20) in the $n_h \rightarrow 0$ limit has been used to rewrite the mode frequency ω_2 , and it is implicitly assumed that time is scaled as given in Eq. (81). Likewise the transport equation takes the form

$$\frac{\partial n_h}{\partial t'} + [n_h, h] + \frac{\partial}{\partial p} \left[-\dot{p}|_T n_h + D' \frac{\partial n_h}{\partial p} \right] = 0. \quad (83)$$

Completing the description, Eqs. (24) and (25) take the form

$$\frac{1}{R_c} \frac{dD_2}{dt'} = -\frac{e}{|e|} \int_0^\pi \frac{d\bar{\theta}_2}{\pi} \int_1^{(R_w/R_c)^2} \frac{dp}{p} \left[1 - \left(\frac{R_c}{R_w} \right)^4 \right] \frac{n_h(\bar{\theta}_2, p, t)}{n_c} \sin 2\bar{\theta}_2 \quad (84)$$

$$\frac{D_2}{R_c} \frac{d\alpha_2}{dt'} = \frac{e}{|e|} \int_0^\pi \frac{d\bar{\theta}_2}{\pi} \int_1^{(R_w/R_c)^2} \frac{dp}{p} \left[1 - \left(\frac{R_c}{R_w} \right)^4 \right] \frac{n_h(\bar{\theta}_2, p, t)}{n_c} \cos 2\bar{\theta}_2. \quad (85)$$

A numerical solution to transport equation (83) can be obtained using a

Langevin scheme²⁸ in which the halo density is represented as a sum of M

discrete line charges

$$\begin{aligned} n_h(\bar{\theta}_2, p, t') &= \lambda \sum_{j=1}^M \frac{\delta[r - r_j(t')]}{r} \delta[\bar{\theta}_2, \bar{\theta}_{2j}(t')] \\ &= \lambda \frac{2}{R_c^2} \sum_{j=1}^M \delta[p - p_j(t')] \delta[\bar{\theta}_2, \bar{\theta}_{2j}(t')], \end{aligned} \quad (86)$$

where λ is the charge per unit length for each line charge. For an arbitrarily small time step $\Delta t'$ each line charge would be advanced according to the equations

$$\Delta p_j = \left(-\frac{\partial h}{\partial \bar{\theta}_{2j}} + \dot{p}|_T - \frac{\partial D'}{\partial p_j} \right) \Delta t' + \sqrt{2D' \Delta t'} N[0, 1], \quad (87)$$

$$\Delta \bar{\theta}_{2j} = \left(\frac{\partial h}{\partial p_j} \right) \Delta t', \quad (88)$$

where the function $N[0, 1]$ is a normal-distributed random variable with zero

mean and unit variance. In fact, for computational efficiency we don't use this lowest order algorithm; rather the two terms that are linear in $\Delta t'$ are replaced by a sixth order Runge Kutta algorithm²⁹ and then the small random step associated with diffusion is added in. To properly resolve the rapid $\mathbf{E} \times \mathbf{B}$ -drift flow, the time step must be much smaller than unity. Since the orbits are symmetric about $\bar{\theta}_2 = \pi$, we only need to follow particles in the domain $0 \leq \bar{\theta}_2 \leq \pi$. A line charge that reaches $\bar{\theta}_2 = \pi$ with angular momentum p is re-inserted at $\bar{\theta}_2 = 0$ with angular momentum p , and vice versa.

Physically, the halo particles emerge from the core through transport, but in the presence of a wave, the surface of the core oscillates back and forth. To avoid the numerical complication of ejecting halo particles from a moving surface, a simple artifice is used. The halo particles are injected at $r = 0$, where the wave amplitude is zero. In the core region, we allow transport (mobility) to act only on the halo particles. From Section IV recall that for constant $\dot{p}|_T$, the combined mobility and $\mathbf{E} \times \mathbf{B}$ -drift flow is incompressible.

Thus, the halo expands at constant density n_h out past the surface of the core, and this constant density makes no contribution to the integrals for the damping rate and frequency shift. The density in the halo region is sufficiently smooth that diffusion is unimportant. In this treatment, the core particles have unperturbed density $n_c - n_h$, and a perturbed density at the surface due the linearized $\mathbf{E} \times \mathbf{B}$ -drift flow from the wave potential. This surface charge density is already included in Eqs. (24) and (25) for the damping rate and frequency shift.

In Eq. (86) the number of line charges M depends on how far the halo has expanded radially. A maximum value, M_{\max} , is required for the case where the halo is allowed to expand all the way to the wall without launching a wave. For this situation the halo density takes the constant value n_h from $r = 0$ to $r = R_w$, so we find a simple relationship between the line density and M_{\max} : $\lambda M_{\max} = \pi R_w^2 n_h$. Of course, M_{\max} must be chosen large enough that discreteness effects are small. Substituting this expression for λ into

Eq. (86) and then substituting the result into Eqs. (84) and (85) yields the expressions

$$\frac{1}{R_c} \frac{dD_2}{dt'} = -\frac{e}{|e|} \frac{n_h}{n_c} \frac{2}{M_{\max}} \left(\frac{R_c}{R_w} \right)^2 \sum_{j=1}^M \frac{1 - (R_c/R_w)^4 p_j^2}{p_j} \sin 2\bar{\theta}_{2j}, \quad (89)$$

$$\frac{D_2}{R_c} \frac{d\alpha_2}{dt'} = \frac{e}{|e|} \frac{n_h}{n_c} \frac{2}{M_{\max}} \left(\frac{R_c}{R_w} \right)^2 \sum_{j=1}^M \frac{1 - (R_c/R_w)^4 p_j^2}{p_j} \cos 2\bar{\theta}_{2j}. \quad (90)$$

The variables $D_2(t')/R_c$, $d\alpha_2/dt' = \Delta\omega(t')/|\omega_E(R_c)|$, $p_j(t')$ and $\bar{\theta}_{2j}(t')$ are dependent variables to be solved for in the numerical solution, but there are other dimensionless quantities in Eqs. (87) to (90) that must be given a numerical value before proceeding to a numerical solution. Consistent with the experiments, we choose the value $R_c/R_w = 0.39$. The ratio n_h/n_c has the value 10^{-2} for all of the experiments. The ratio $\dot{p}|_T = \dot{P}_\theta|_T/Ne^2$ depends on the strength of the applied field asymmetry used to control the transport flux. We select the value 2.2×10^{-6} for our numerical solutions. This choice is motivated by the experimental parameters, $R_w = 3.5\text{cm}$, $B = 12\text{kG}$ and $\dot{N} = 1.35\text{s}^{-1}$. To include the effect of small diffusion, the approximate experimental

value $T/Ne^2 = 3 \times 10^{-3}$ is used.

To further smooth out the effect of discrete line charges, we use the running averages

$$\left\langle \frac{dD_2}{dt'} \right\rangle(t') = \frac{1}{N_{\text{avg}}} \sum_{j=0}^{N_{\text{avg}}-1} \frac{dD_2}{dt'}(t' - j\Delta t'), \quad (91)$$

$$\left\langle \frac{d\alpha_2}{dt'} \right\rangle(t') = \frac{1}{N_{\text{avg}}} \sum_{j=0}^{N_{\text{avg}}-1} \frac{d\alpha_2}{dt'}(t' - j\Delta t'). \quad (92)$$

The value of N_{avg} is chosen to be large enough to smooth out discreteness fluctuations, but still small enough that $N_{\text{avg}}\Delta t'$ is small compared to the time scale on which the averaged quantities vary. The average quantities are used in Hamiltonian (82) and transport equation (83).

Here we present results from a numerical simulation using the chosen parameter values and compare with the theory in Section 5. The scaled amplitude D_2/R_c takes an initial value of 0.05. D_2 and $\dot{\alpha}$ are evolved using Eqs. (91) and (92). The halo density is advanced forward by mobility and small diffusion as explained above.

The solid dots in Fig. (4) show the simulation results for $D_2(t)/R_c$ versus $|\dot{N}t|N$ for the initial condition $D_2(0)/R_c = 0.05$. The dashed curve is the numerical solution of Eq. (71) and Eq. (74) assuming the same initial condition and the same value of the density ratio $n_h/n_c = 0.01$. The two curves are in good agreement. The solid curve follows the experimental observed damping rate in Eq. (2).

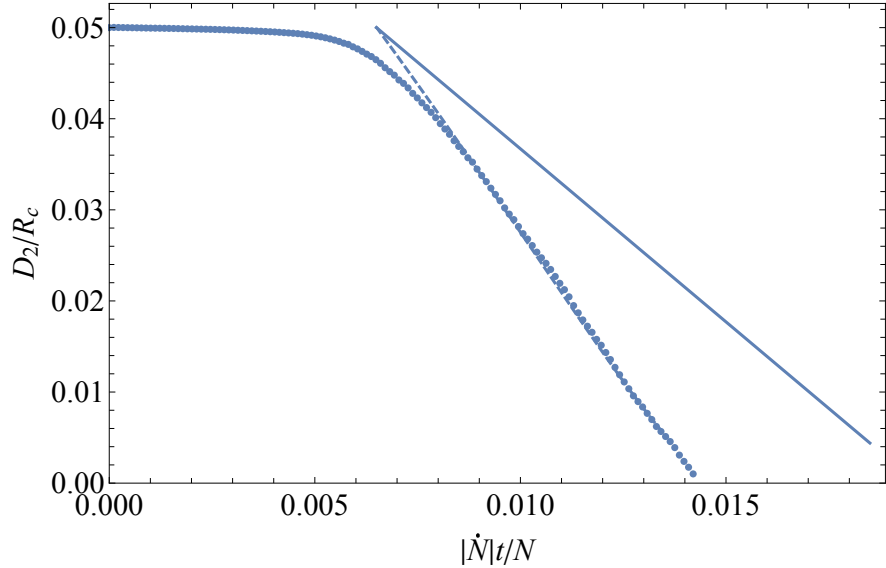


Figure 4: \dot{D}_2 as a function of t for the simulation. The solid dots are results from the simulation. The solid curve is the damping curve for Eq. (2) with the damping rate taking experimentally observed value. The dashed curve followed from numerical solution of Eq. (74) using $n_h/n_c = 0.01$.

Fig (5) is the plot of the scaled frequency shift versus $|\dot{N}t|N$ for the initial

condition $D_2(0)/R_c = 0.05$, with the dots representing the simulation results and the solid curve obtained from Eq. (80). Again, there is reasonably good agreement.

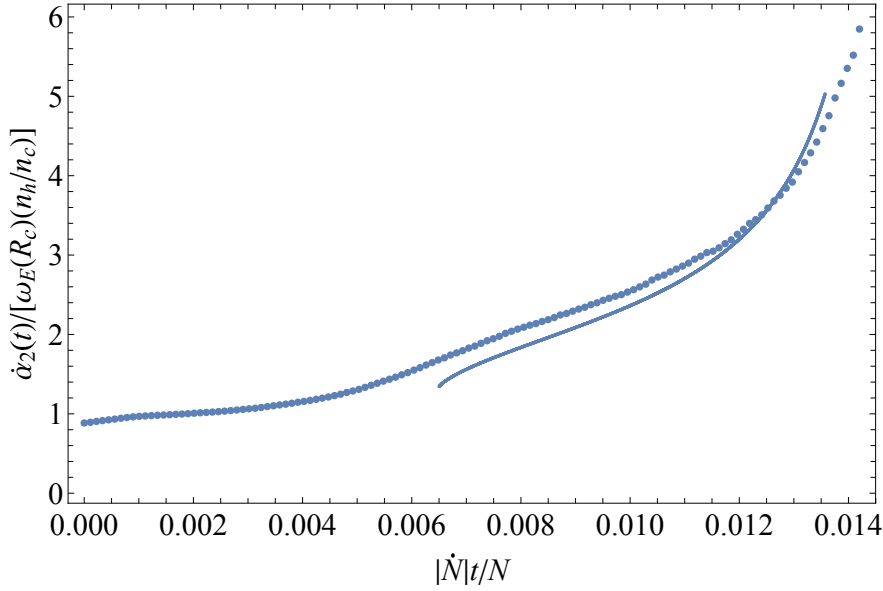


Figure 5: Plot of $\dot{\alpha}_2$ against t obtained in the simulation (blue dots) and expected results (solid curve).

Fig. (6) shows the distribution of line charges near the critical radius at the instant that $D_2/R_c = 0.02$, with the dashed curved being the critical contour of a top-hat core with the same R_c and N . Note that the line charges are slightly less dense on the side of larger $|p|$ in Fig. (6). Recall from Section 4 that the incorrect assumption of constant mode amplitude led to an erroneous conclusion that the density on the two sides of the cat's eye region would be

the same.

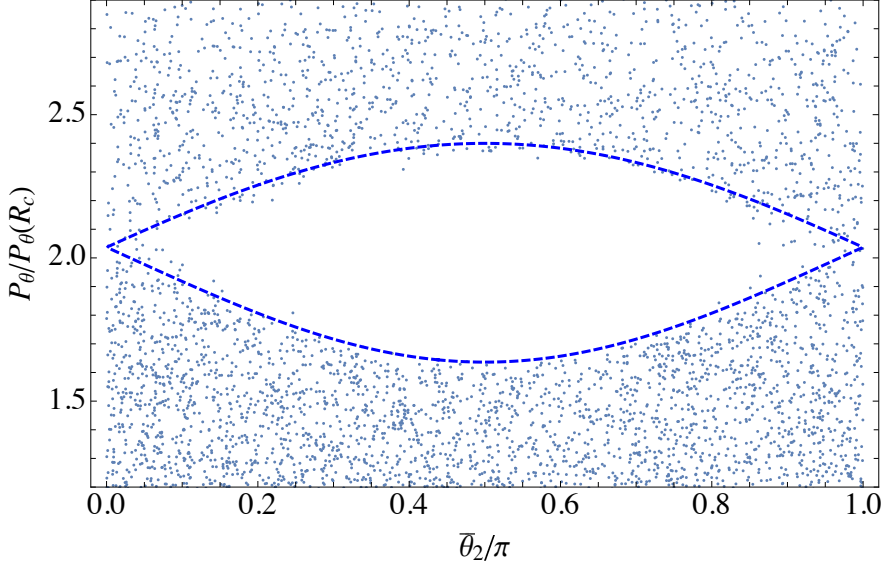


Figure 6: Plot of line charges near the cat's-eye orbit at $D_2/R_c = 0.02$. The blue dots are the line charges and the blue dashed curve is the critical contour of h for a top-hat core density profile.

To understand the reason for the difference in charge density between the two sides, we study an extreme case and plot the line charges in the $(\bar{\theta}_2, p)$ -plane near the critical contour at a much greater resolution. The Hamiltonian in Eq. (82) is used with the frequency shift adjustment $\Delta\omega = 0$. We set λ to be much lower and $\dot{P}_\theta|_T$ to be higher than usual so that the fine structures of the halo flow can be seen in the figure. We set $D' = 0$ so that the fine halo structure is not diffusely broadened. Also, in order to focus on the region near

the critical contour and save computational power, we inject line charges at a constant- h contour near the critical contour. For the case where D_2 is allowed to vary with time, the injection contour is chosen to be area-preserving to keep the flow incompressible.

Fig. (7) shows the flow of line charges in blue dots for the time-independent case, for $D_2/R_c = 0.05$. The red line is the critical contour of h . The green line is the injection contour. Line charges are swept around the critical contour, forming filament segments that stack tightly with each other, and thus form a halo of equal density on either side of the cat's-eye region. Fig. (8) on the other hand shows the same distribution for the case where D_2 is set to decrease at a slow rate. For this case we see that gaps form in between the filament segments. This is not surprising since particles do not follow constant Hamiltonian contours if h is time-dependent. Even small diffusion smooths out the filamentary structure but leaves a lower density as shown in Fig. (6).

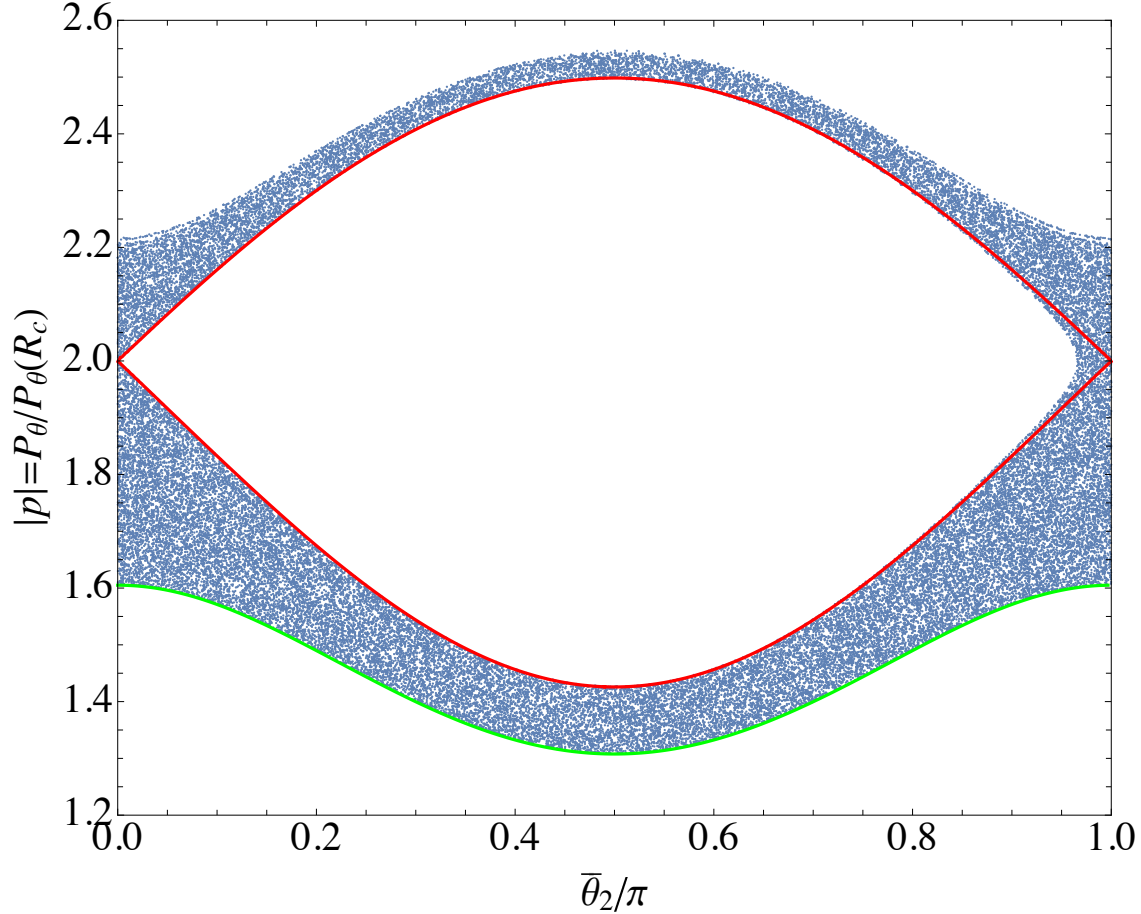


Figure 7: Plot of line charges (blue dots) following a time-independent h from Eq. (82) for $D_2/R_c = 0.05$.

The red line is the critical contour of h , and the green line is the injection contour.

Finally, the 30% difference between the theoretical and experimental damping rates in Fig. (4) is not surprising considering the coarseness of the top hat model and the possible inaccuracy in measurement of the halo flux. In spite of the coarseness, the theory does capture the two striking signatures of the flux driven damping; namely that the damping begins when the halo

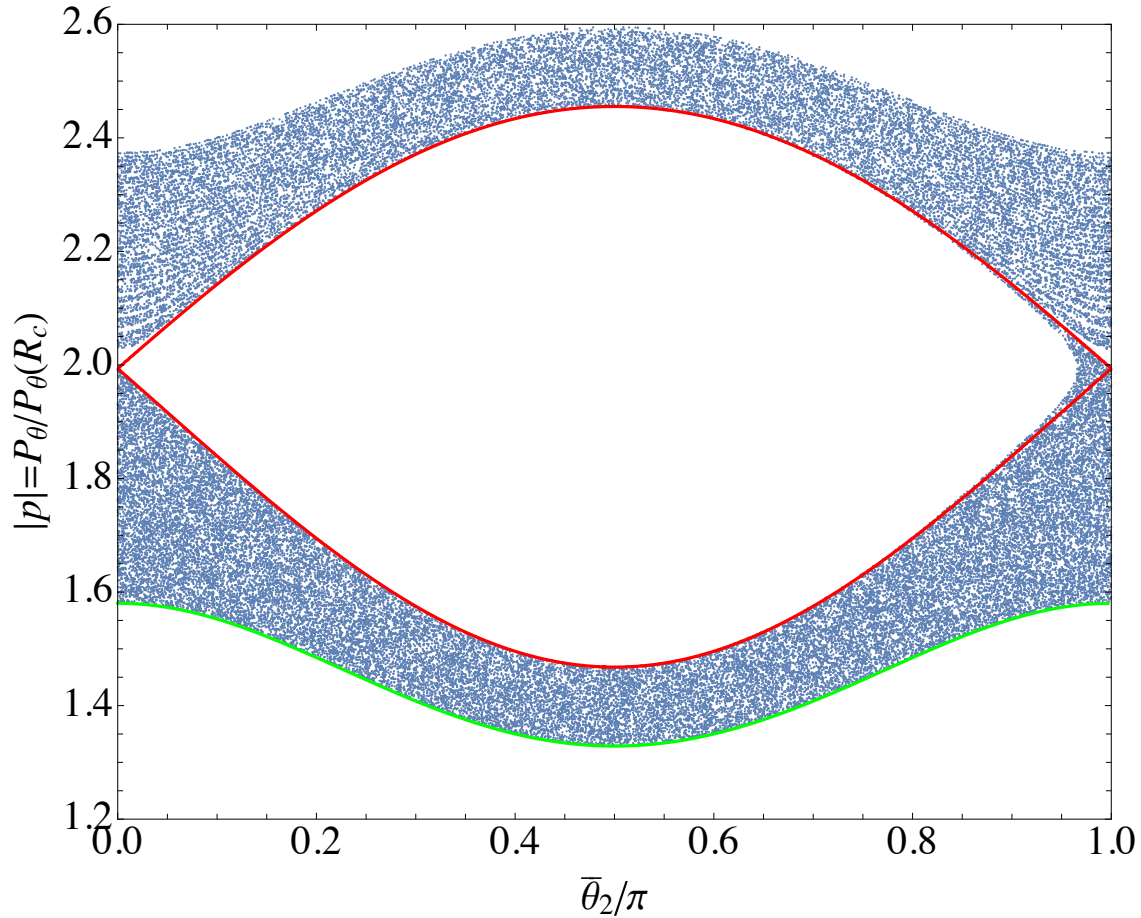


Figure 8: Plot of line charges (blue dots) following a time-dependent h from Eq. (82) for $D_2/R_c = 0.05$.

The red line is the critical contour of h , and the green line is the injection contour.

particles reach the resonant radius and that the damping is algebraic in time

with nearly constant damping rate.

References

- [1] R. C. Davidson, *Physics of nonneutral plasmas*, chapter 6, pp. 289–343, Imperial College Press, 2001.
- [2] R. Levy, Phys. Fluids **8**, 1288 (1965).
- [3] C. Driscoll and K. Fine, Phys. Fluids B **2**, 1359 (1990).
- [4] J. Fajans, E. Gilson, and L. Friedland, Phys. Rev. Lett. **82**, 4444 (1999).
- [5] R. Briggs, J. Daugherty, and R. Levy, Phys. Fluids **13**, 421 (1970).
- [6] N. Balmforth, S. G. L. Smith, and W. Young, J. Fluid Mech. **426**, 95 (2001).
- [7] W. D. White, J. H. Malmberg, and C. F. Driscoll, Phys. Rev. Lett. **49**, 1822 (1982).
- [8] R. C. Davidson and E. H. Chao, Phys. Plasmas **3**, 3279 (1996).
- [9] A. Kabantsev and C. Driscoll, Fus. Sci. and Tech. **51**, 96 (2007).

- [10] D. Schecter, D. Dubin, A. Cass, C. Driscoll, I. Lansky, and T. O’Neil, Phys. Fluids **12**, 2397 (2000).
- [11] S. Crooks and T. O’Neil, Phys. Plasmas **2**, 355 (1995).
- [12] B. Cluggish and C. Driscoll, Phys. Rev. Lett. **74**, 4213 (1995).
- [13] E. Sarid, E. P. Gilson, and J. Fajans, Phys. Rev. Lett. **89**, 105002 (2002).
- [14] A. Kabantsev, C. Driscoll, T. Hilsabeck, T. O’Neil, and J. Yu, Phys. Rev. Lett. **87**, 225002 (2001).
- [15] A. Kabantsev, C. Chim, T. O’Neil, and C. Driscoll, Phys. Rev. Lett. **112**, 115003 (2014).
- [16] A. A. Kabantsev, K. A. Thompson, and C. F. Driscoll, First experiments with e/h plasmas: Enhanced centrifugal separation from diocotron mode damping, in *AIP Conf. Proc.*, volume 1928, p. 020008, 2018.
- [17] D. L. Eggleston and T. M. O’Neil, Phys. Plasmas **6**, 2699 (1999).
- [18] T. M. O’Neil, Phys. Fluids **23**, 2216 (1980).

- [19] T. M. O’Neil and R. A. Smith, Phys. Fluids B **4**, 2720 (1992).
- [20] C. Y. Chim and T. M. O’Neil, Flux-driven algebraic damping of dielectric modes, in *NON-NEUTRAL PLASMA PHYSICS IX: 11th International Workshop on Non-Neutral Plasmas*, edited by H. Himura, A. Sanpei, and Y. Soga, volume 1668, p. 020004, AIP Publishing, 2015.
- [21] C. Y. Chim and T. M. O’Neil, Phys. Plasmas **23**, 072113 (2016).
- [22] C. Y. Chim and T. M. O’Neil, Phys. Plasmas **23**, 050801 (2016).
- [23] J. Taylor, Phys. Fluids **7**, 767 (1964).
- [24] T. O’Neil and R. Smith, Phys. Plasmas **1**, 2430 (1994).
- [25] H. Goldstein, C. Poole, and J. Safko, *Classical mechanics*, chapter 8, pp. 334–367, Addison–Wesley, 3rd edition, 2002.
- [26] H. Goldstein, C. Poole, and J. Safko, *Classical mechanics*, chapter 9, pp. 368–429, Addison–Wesley, 3rd edition, 2002.

- [27] M. Balkanski and R. F. Wallis, *Semiconductor physics and applications*, volume 8, chapter 8, pp. 159–160, Oxford University Press, 2000.
- [28] N. Van Kampen, *Stochastic Processes in Physics and Chemistry (Third Edition)*, pp. 52 – 72, North-Holland Personal Library, Elsevier, Amsterdam, third edition, 2007.
- [29] J. C. Butcher, J. Austr. Math. Soc. **4**, 179 (1964).